CARL VON OSSIETZKY universität OLDENBURG

University of Applied Sciences
HOCHSCHULE EMDEN·LEER

From 1D to 3D Vibration Analysis

Periodic In-Plane Motions on a Nanometer Scale based on Optical Flow Analysis

Author:
Henri GODE

Supervisors:
Prof. Dr. Walter NEU
Dr. Iwan SCHAAP

Bachelor Thesis

Engineering Physics

at SmarAct GmbH

SmarAct
PERFECT MOTION

January 3, 2019

Acknowledgment

Firstly, I want to thank and honor God, who indeed gave me the abilities, opportunities, strength and creativity to accomplish this work. Additionally, I am very grateful for the opportunity to work on this project within the company SmarAct GmbH in Oldenburg, where I got a working place with access to the necessary instruments and support in any question. Also, I appreciate the following persons for their support and encouragement during this work:

- Prof. Dr. Walter Neu (Supervising Professor at University Oldenburg)
- Dr. Iwan Schaap (Supervisor at SmarAct and PICOSCAN Vibrometer project leader)
- Dr. Sebastian Rode (Head of Metrology Department at SmarAct GmbH)
- Dr. Christoph Baune (Application Engineer at SmarAct GmbH)
- Michael Lherbette (Application Engineer at SmarAct GmbH)
- Vincent Hamann (High Level Software Developer at SmarAct GmbH)
- Marcel Derleh (Low Level Software Developer at SmarAct GmbH)
- Benjamin Schmidt (Low Level Software Developer at SmarAct GmbH)
- Norbert Kwiatkowski (Electrical Engineer at SmarAct GmbH)
- Bernd Kramer (Electrical Engineer at SmarAct GmbH)

Contents

Abbreviations

AFM atomic force microscopy

CCD charge-coupled device

DDS direct digital synthesizer

EC error correlation

FFT fast Fourier transform

FPGA field programmable gate array

FT-G6o Femtotools FT-G6o Microgripper

FWHM full width at half maximum

KE knife edging

LIA lock-in amplifier

MEMS micro-electro-mechanical system

OFEPIS optical flow estimation for a periodic image sequence

PSV PICOSCAN Vibrometer

ROI region of interest

SPM sinusoidal phase modulation

STD standard deviation

TM template matching

List of Figures

Chapter 1

Introduction and Motivation

This bachelor project is based on SmarAct's PICOSCAN Vibrometer (PSV), which is currently developed to investigate out-of-plane vibrations of sample surfaces based on sinusoidal phase modulation (SPM)-interferometry. A built in lock-in amplifier (LIA) enables the instrument to extract the amplitude and phase of the vertical vibration of the investigated surface with picometer accuracy. Therefore it can be used investigate the dynamic response of different samples such as atomic force microscopy (AFM) cantilevers, mobile phone loudspeakers or micro-electro-mechanical system (MEMS). The revealed dynamic response can then be used to characterize the quality and understanding of it allows to tune the product to a wanted performance. This project aims to extend the instrument to offer investigations of vibrations in all 3 dimensions, thus also in-plane-vibrations. These lateral vibrations are often coupled with the vertical vibrations and it is of great advantage to know the complete vibrational behavior in 3D space in order to understand motion and function of the investigated sample. Since the product was already about to be released its hardware should not be changed at all and firmware modifications should be minor. Due to these limiting conditions I needed to realize this project by developing a post-processing software, which processes the measurement data. In order to get this required information also a different recording process of data needed to be developed as pre-processing. Based on its SPM-interferometry the PSV offers scanning of confocal microscopy images. Taking advantage of the principle of stroboscopic imaging allowed me to construct periodic image sequences, which contained exactly one period of the actuated sine wave. In order to provide the data for the analysis software a method of simultaneously measuring the reflection and referencing it to the momentary angular phase of the actuating signal was developed and realized in the firmware of the PSV.

The main part of the project was implementing and optimizing different methods to extract lateral vibration information out of this image sequences. Therefor I developed an analysis software, which constructs the image sequence and is able to perform different techniques based on various image processing and fitting algorithms. Hereby I aimed to measure down to 10 nm vibrations amplitudes, which is about 100 times smaller than the pixel resolution and about 500 times smaller than the optical resolution. This main approach of the template matching (TM) on a periodic image sequence was inspired by Cretin et al. [1].

Chapter 2

Physical Principles of Vibration Measurement

Here I describe the fundamental theories, methods and algorithms, on which this work is based. The following list provides the topics and their application or usage in this work:

- The theory about flexural vibrations of free rectangular beams can describe the dynamic behavior of the samples in order to compare the theoretical results to the measured data.
- The principles of SPM interferometry is used by the PSV to provide accurate position and reflection intensity data.
- Temporal and spatial image derivatives are computed by convolution with derivative kernels and they are used by all approaches to estimation the motion.
- The 2D weighted least square peak fitting algorithm is used to reveal the sub-pixel position of optimal correlation position of two images.
- The Lucas-Kanade algorithm can give a rough estimate of image motion for every pixel.
- The optical flow estimation for a periodic image sequence (OFEPIS) algorithm can reveal vibrations by estimating the periodic motion at each pixel.

2.1 Flexural Vibrations of Free Rectangular Beams

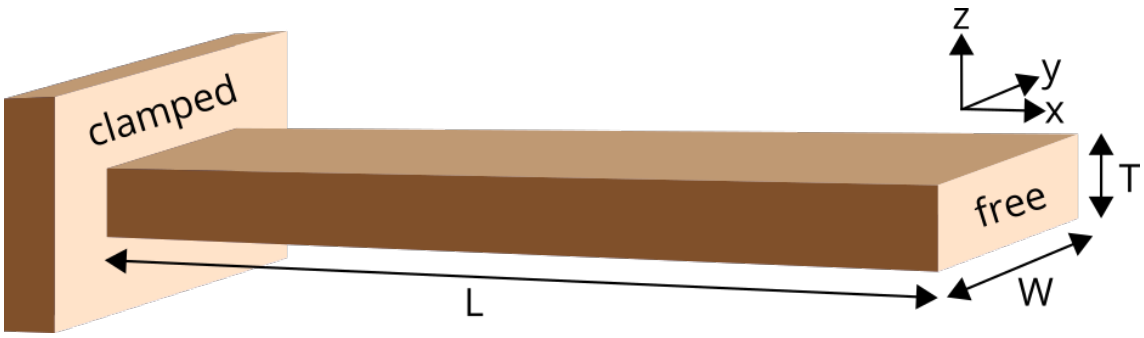

Figure 2.1: Rectangular free Euler-Bernoulli beam. Dimensions given by length L, width W and thickness T. Horizontal flexural vibrations are defined to oscillate in y-direction and vertical flexural vibrations in z-direction.

This section describes the vibrational behavior of beams, since the theory allows selection of suitable samples by revealing their resonance frequencies and bending shapes and it allows to interpret the results by comparing it to the theoretical model. The dynamic behavior of rectangular beams, which are mounted at one end and free at the other, can be described by Euler-Bernoulli beam theory, if the beams cross section $A = W \cdot T$, second moment of inertia I, elasticity module E and density ρ are approximately uniform. For rectangular shaped beams the vertical second moment of inertia is given by $I_z = W \cdot T^3/12$ and the horizontal by $I_y = T \cdot W^3/12$. An analytic solution of the displacement z depending on position x, time t, amplitude M and frequency f can be determined based on a forth order differential equation [2], [3]:

$$E \cdot I \cdot \frac{\partial^4 z(x,t)}{\partial x^4} + \rho \cdot A \cdot \frac{\partial^2 z(x,t)}{\partial t^2} = 0 \tag{2.1}$$

A general solution to Equation 2.1 is given by:

$$z(x,t) = \left(\alpha_1 \cdot e^{kx} + \alpha_2 \cdot e^{-kx} + \alpha_3 \cdot e^{ikx} + \alpha_4 \cdot e^{-ikx}\right) e^{-i\omega t} \tag{2.2}$$

Inserting Equation 2.2 into Equation 2.1 results in the dispersion relation:

$$EI \cdot k^4 - \rho A \cdot \omega^2 = 0 \quad \Leftrightarrow \quad 2\pi \cdot f = \omega = k^2 \sqrt{\frac{EI}{\rho A}} \tag{2.3}$$

Since one end of the cantilever beam is clamped (e.g. to a wafer-chip), it is not able to move and the displacement and slope at this end must be zero. At the free end of

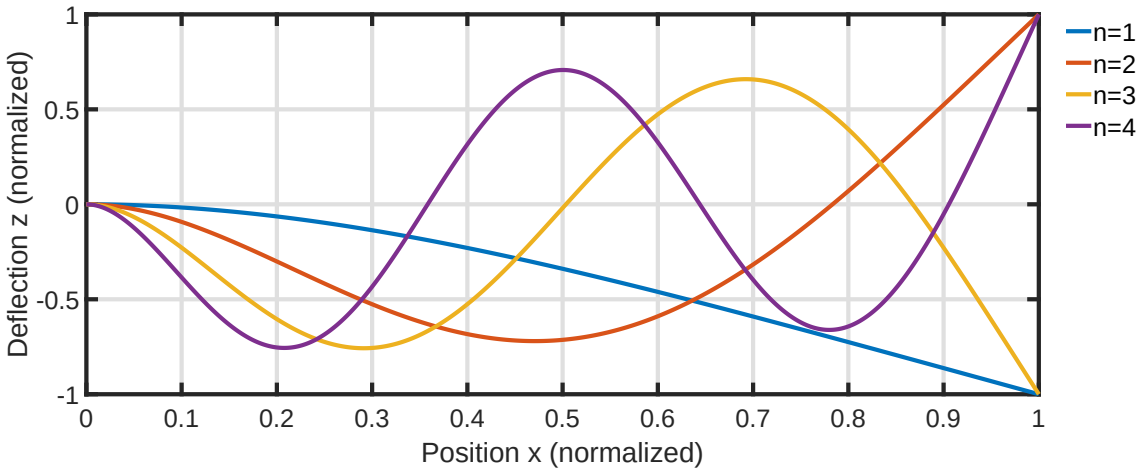

Figure 2.2: First four flexural vibration modes of Euler-Bernoulli beam.

the cantilever there is no moment or shear force. This results in the following boundary conditions in Equation 2.4 for a cantilever with a clamped and a free end:

$$\begin{aligned} z(0,t) = 0, \quad \frac{\partial z(0,t)}{\partial x} = 0 \quad (\text{clamped at} \quad x = 0) \\ \text{and} \quad \frac{\partial^2 z(0,t)}{\partial x^2} = 0, \quad \frac{\partial^3 z(0,t)}{\partial x^3} = 0 \quad (\text{free at} \quad x = L) \end{aligned} \tag{2.4}$$

These four equations gained by the boundary conditions are solved for the coefficients $\alpha_i \quad (i = 1,2,3,4)$. Solutions only exist, if the characteristic equation

$$\cos(k_n L)\cosh(k_n L) + 1 = 0 \tag{2.5}$$

is fulfilled. This condition leads to an infinite set of discrete solutions for $k_n L$, whereby each corresponds to a flexural vibration mode with mode number $n \in \mathbb{N}$, wave number k_n and frequency f_n (calculated by the dispersion relation in Equation 2.3). Inserting the allowed solutions and the determined coefficients into the general solution results in the deflection

$$z_n(x) = M\left(\cos(k_n x) - \cosh(k_n x) - \frac{\cos(k_n L) + \cosh(k_n L)}{\sin(k_n L) + \sinh(k_n L)}\left[\sin(k_n x) - \sinh(k_n x)\right]\right) \tag{2.6}$$

for all mode numbers n. Figure 2.2 shows the first four flexural vibration modes of an Euler-Bernoulli beam calculated by Equation 2.6.

2.2 Sinusoidal Phase Modulation Interferometry

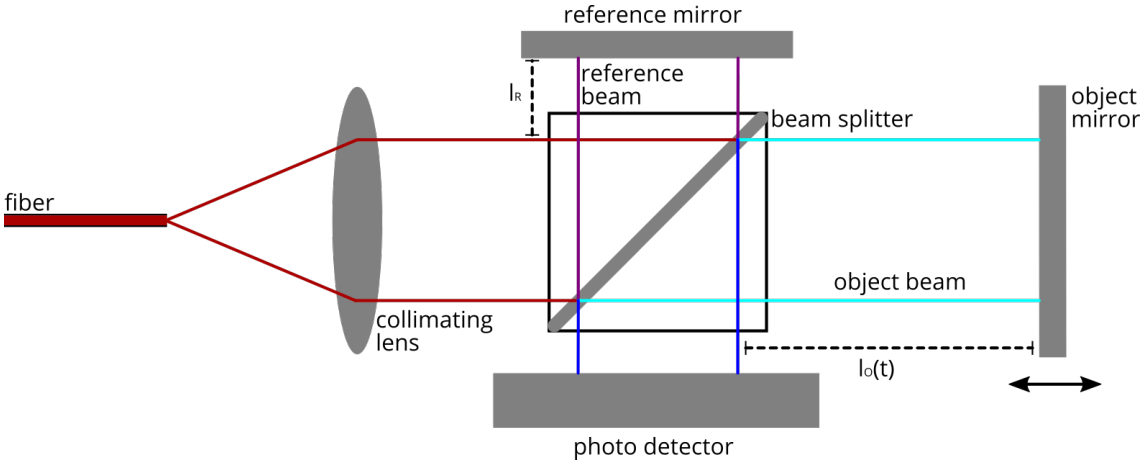

Figure 2.3: Schematic setup of a Michelson interferometer.

SPM interferometry is here explained based on a Michelson interferometer setup [4], [5] seen in Figure 2.3. A single mode optical fiber outputs a light beam of wavelength λ, which is collimated by a lens. A beam splitter separates the beam into a reference beam and an object beam, which are reflected each by its respective mirror. After passing through the beam splitter again, both reflected beams interfere. A photo detector measures the intensity of the recombined beam. The "time of flight" of the object and reference beam (τ_O,τ_R) is given by the path lengths (l_O,l_R) and the speed of light c assuming the refractive index of the environment $n_{AIR} \approx 1$.

$$\tau_O(t) = \frac{2l_O(t)}{c} \quad \text{and} \quad \tau_R = \frac{2l_R}{c} \tag{2.7}$$

Usually the reference mirror is fixed so that l_R and τ_R are constant, however the object mirror (here it is the reflective surface of the investigated samples) is movable so that l_O and τ_O depend on time t. The reference and object beam can be described by sinusoidal waves $U_O(t)$ and $U_R(t)$, which interfere depending on the optical path difference, only if the coherence length is larger than the optical path difference $L_c \gg n(l_O - l_R)$. In general, ω depends on time so that the waves are defined as:

$$\begin{aligned} U_O(t) &= \alpha_O \sin\left(\Phi_O(t)\right) \quad \text{with} \quad \Phi_O(t) = \int_0^{t-\tau_O(t)} \omega(t)dt = 2\pi c \int_0^{t-\tau_O(t)} \frac{1}{\lambda(t)}dt \\ U_R(t) &= \alpha_R \sin\left(\Phi_R(t)\right) \quad \text{with} \quad \Phi_R(t) = \int_0^{t-\tau_R} \omega(t)dt = 2\pi c \int_0^{t-\tau_R} \frac{1}{\lambda(t)}dt, \end{aligned} \tag{2.8}$$

whereby α_O and α_R represent the amplitudes of the light waves (e.g. the electric field strength). The interference light wave is given by the superposition of the two oscillating wave vectors $U_O(t)$ and $U_R(t)$:

$$\begin{aligned} U(t) &= \alpha_O \sin(\Phi_O(t)) + \alpha_R \sin(\Phi_R(t)) \\ U(t) &= U_0 \sin(\Phi) \\ \text{with} \quad U_0 &= \sqrt{{\alpha_O}^2 + {\alpha_R}^2 + 2\alpha_O\alpha_R \cos(\Phi_R - \Phi_O)} \\ \text{and} \quad \Phi &= \arctan\left(\frac{\alpha_O \sin(\Phi_O) + \alpha_R \sin(\Phi_R)}{\alpha_O \cos(\Phi_O) + \alpha_R \cos(\Phi_R)}\right) \end{aligned} \tag{2.9}$$

However the photo detector is not able to detect the high frequency ω of the light, so that it measures the averaged intensity $I(t)$, which for electromagnetic, plane waves is described by [6]:

$$\begin{aligned} I(t) &= \frac{c\epsilon_0 {U_0}^2}{2} \quad \Rightarrow \quad I(t) \propto {U_0}^2 \\ I(t) &= I_O + I_R + 2\sqrt{I_O I_R}\cos(\Phi_R - \Phi_O) \end{aligned} \tag{2.10}$$

The visibility $V = \frac{2\sqrt{I_O I_R}}{I_0}$ (also called fringe contrast), which describes the contrast of the interferometer signal, is inserted into Equation 2.10:

$$\begin{aligned} I(t) &= I_0 + V \cdot I_0 \cos(\Delta\Phi) \\ \text{with} \quad I_0 &= I_O + I_R \quad \text{and} \quad \Delta\Phi = \Phi_R - \Phi_O \end{aligned} \tag{2.11}$$

Operating the Michelson interferometer with a constant wavelength λ simplifies the phases of the two waves from Equation 2.8 to:

$$\Phi_O = \frac{2\pi c(t - \tau_O)}{\lambda} \quad \text{and} \quad \Phi_R = \frac{2\pi c(t - \tau_R)}{\lambda}, \tag{2.12}$$

which by using Equation 2.7 results in:

$$\Delta\Phi = \Phi_R - \Phi_O = \frac{2\pi(\tau_O - \tau_R)}{\lambda} = \frac{4\pi(l_O - l_R)}{\lambda} \tag{2.13}$$

So the intensity measured by the photo diode depends only on the optical path difference

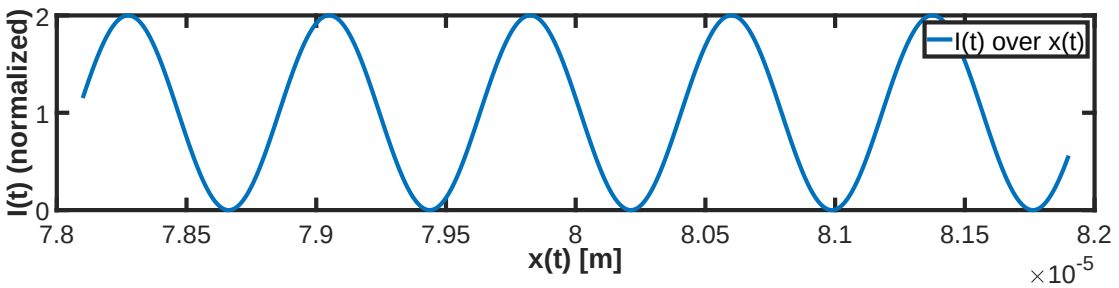

Figure 2.4: Intensity I(t) measured by the photo detector while the object path difference x(t) increases. (for $\lambda(t) = 1550\,\text{nm} = const.$)

$x(t) = l_O(t) - l_R$ (inserting Equation 2.13 into Equation 2.11):

$$I(t) = I_0 + V \cdot I_0 \cos\left(\frac{4\pi}{\lambda} x(t)\right) \tag{2.14}$$

Therefore, operating the Michelson interferometer with a constant wavelength yields in a sinusoidal signal, which does not provide information about the direction, whenever an intensity maximum or minimum is measured with the photo detector (see Figure 2.4). Additionally, the intensity at the photo detector depends on the optical path difference $x(t)$, which disables measuring the reflectance of the objects surface. These two issues are solved by SPM interferometry which is based on a sinusoidal wavelength modulation. By alternating the drive current of the laser diode with a modulation frequency ω_m, the wavelength can be described by:

$$\lambda(t) = \lambda_0 + \Delta\lambda(t) = \lambda_0 + \Delta\lambda_0 \cos(\omega_m t), \tag{2.15}$$

whereby λ_0 is the center wavelength and $\Delta\lambda_0$ is the modulation amplitude of the wavelength. In order to analytically solve the integrals in Equation 2.8 the following approximation holds for $\Delta\lambda \ll \lambda_0$:

$$\frac{1}{\lambda(t)} = \frac{1}{\lambda_0 + \Delta\lambda(t)} \approx \frac{1}{\lambda_0}\left(1 - \frac{\Delta\lambda(t)}{\lambda_0}\right) \tag{2.16}$$

Using Equation 2.8, Equation 2.15, Equation 2.16 and trigonometric identities gives the phase difference $\Delta\Phi(t)$ of the SPM interferometry as [6], [7], [8]:

$$\Delta\Phi(t) = \frac{4\pi}{\lambda_0}(l_O - l_R) - \frac{4\pi c \Delta\lambda}{\omega_m {\lambda_0}^2} \sin\left(\frac{\omega_m(\tau_O - \tau_R)}{2}\right) \cos\left(\omega_m t - \frac{\omega_m(\tau_O + \tau_R)}{2}\right) \tag{2.17}$$

Inserting this into Equation 2.11 leads to the following intensity function, describing the

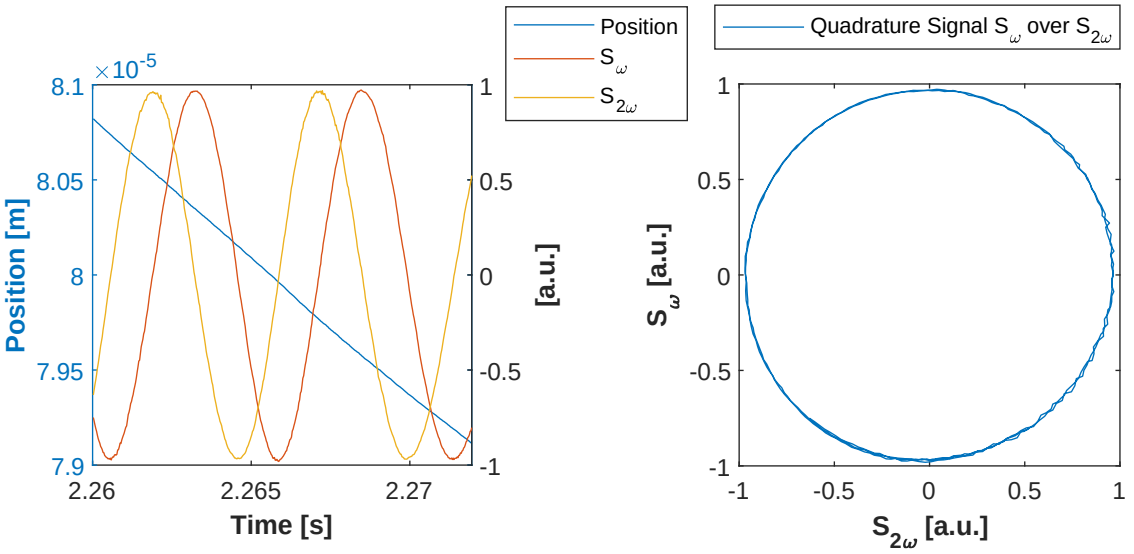

Figure 2.5: Recorded S_ω and $S_{2\omega}$ extracted from a LIA while the object moves towards the beam splitter. a) S_ω, $S_{2\omega}$ and the calculated relative position $x(t)$ are plotted over time ($\lambda_0 = 1550\,\text{nm}$). b) S_ω is plotted over $S_{2\omega}$ in a Lissajous plot.

signal measured by the photo diode:

$$\begin{aligned} I(t) &= I_0 + V I_0 \cos\left[z\cos\left(\omega_m t + \varphi\right) + \theta\right] \\ \text{with} \quad z &= -\frac{4\pi c \Delta\lambda}{\omega_m {\lambda_0}^2} \sin\left(\frac{\omega_m(\tau_O - \tau_R)}{2}\right) \\ \text{and} \quad \theta &= \frac{4\pi}{\lambda_0} x(t) \quad \text{and} \quad \varphi = -\frac{\omega_m(\tau_O + \tau_R)}{2} \end{aligned} \tag{2.18}$$

where z is the modulation depth, θ is a phase offset, which is constant for a fixed optical path length difference $x(t) = l_O(t) - l_R$ and independent of the modulation frequency ω_m and φ describes a phase offset of the AC component of the phase modulation. Equation 2.18 can be expanded using Bessel functions $J_k(z)$ of the first kind of the modulation depth z:

$$\begin{aligned} I(t) &= I_0 + V I_0 [S_{DC} + S_\omega \cos(\omega_m t + \varphi) + S_{2\omega}\cos(2\omega_m t + 2\varphi) \\ &\quad + S_{3\omega}\cos(3\omega_m t + 3\varphi) + S_{4\omega}\cos(4\omega_m t + 4\varphi) + \ldots] \\ I(t) &= I_0 + V I_0 \left[S_{DC} + \sum_{k=1}^{\infty} S_{k\omega}\cos(k\omega_m t + k\varphi)\right] \\ \text{with} \quad S_{DC} &= J_0(z)\cos(\theta) \\ \text{and} \quad S_{k\omega} &= 2J_k(z)\frac{d^k}{d\alpha^k}[\cos(\theta)] \quad \text{for} \quad k \in \mathbb{N}^+ \end{aligned} \tag{2.19}$$

Expanding the intensity signal using the Bessel function is of advantage, because odd harmonics of the modulation frequency ω_m are amplitude modulated by the sine of the phase offset θ and even harmonics are modulated by the cosine of θ. By detecting (appropriate lock-in filtering) of $S_\omega \propto \sin(\theta)$ (odd harmonic) and $S_{2\omega} \propto \cos(\theta)$ (even harmonic), quadrature components of the interferometer phase can be constructed. Figure 2.5 b) shows the Lissajous plot of S_ω over $S_{2\omega}$, seen in Figure 2.5 a), whereby one circumference corresponds to a position change of $\lambda_0/2$. Figure 2.5 a) also shows the relative position $x(t)$ determined by the angle γ of the Lissajous plot:

$$x(t) = \left(\frac{\gamma(t)}{2\pi} + c\right)\frac{\lambda_0}{2} \quad \text{with} \quad \gamma(t) = \arctan 2\left(S_\omega(t), S_{2\omega}(t)\right), \tag{2.20}$$

whereby $c \in \mathbb{Z}$ counts the revolutions of the Lissajous circle to unwrap the angle γ from the arctan2 operation. The quadrature signal also provides information about the direction at any relative position. The radius $R_L = \sqrt{{S_\omega}^2 + {S_{2\omega}}^2}$ of the Lissajous circle in Figure 2.5, which does not depend on the optical path difference $x(t)$, can be interpreted as relative reflectance of the objects surface.

Chapter 3

2D Image Processing

3.1 Image Derivatives

The motion information in a sequence of images lies within its derivatives, as they are the measures of change in respect to space and time. Therefore, the image derivatives are able to emphasize small motions. The image sequence $\mathbf{I}(x, y, t)$ contains the intensity values of the recorded object for every pixel and T time frames $(t = 0 \ \ldots \ T-1)$, which allows calculation of the spatial derivatives $\partial\mathbf{I}/\partial x$, $\partial\mathbf{I}/\partial y$ and the temporal derivative $\partial\mathbf{I}/\partial t$. The spatial derivatives are determined by convolution (indicated by $*$) of each time frame $\mathbf{I_t}$ with derivative kernels. Derivative kernels compute anisotropic image derivatives, since they have a directionality. Here the 5×5 derivative kernels $\mathbf{K_x}$ and $\mathbf{K_y}$ from Kroon [9] are used, which performs better than the Sobel kernels [10], since the signal dependency on the angle is minimized.

$$\mathbf{K_x} = \begin{bmatrix} 0.0007 & 0.0037 & 0 & -0.0037 & -0.0007 \\ 0.0052 & 0.1187 & 0 & -0.1187 & -0.0052 \\ 0.0370 & 0.2589 & 0 & -0.2589 & -0.0370 \\ 0.0052 & 0.1187 & 0 & -0.1187 & -0.0052 \\ 0.0007 & 0.0037 & 0 & -0.0037 & -0.0007 \end{bmatrix} = \mathbf{K_y^T} \tag{3.1}$$

$$\mathbf{I_{\partial x}} = \frac{\partial \mathbf{I_t}}{\partial x} = \mathbf{K_x} * \mathbf{I_t} \quad \text{and} \quad \mathbf{I_{\partial y}} = \frac{\partial \mathbf{I_t}}{\partial y} = \mathbf{K_y} * \mathbf{I_t} \tag{3.2}$$

The magnitudes $\mathbf{I_{spatial}}$ and directions α (angles) of the gradient field can be determined by $\mathbf{I_{\partial x}}$ and $\mathbf{I_{\partial y}}$ as:

$$\mathbf{I_{spatial}} = \sqrt{\mathbf{I_{\partial x}}^2 + \mathbf{I_{\partial y}}^2} \quad \text{and} \quad \alpha = \arctan 2(\mathbf{I_{\partial y}}, \mathbf{I_{\partial x}}) \tag{3.3}$$

The temporal derivative is approximated by the method of finite differences, whereby the central differences are used. The following derivative kernel $\mathbf{D_t}$ in Equation 3.5 is convoluted with the intensity over time at each pixel (x, y). Due to the periodicity of the image sequence one can add the last frame in front of the sequence and the first frame in the end of the sequence to also calculate the derivative values marginal frame.

$$\mathbf{I^+_{x,y}} = \left[I_{x,y,T-1}, I_{x,y,0}, I_{x,y,1}, \cdots, I_{x,y,T-2}, I_{x,y,T-1}, I_{x,y,0}\right] \tag{3.4}$$

$$\mathbf{D_t} = \begin{bmatrix} +1 \\ 0 \\ -1 \end{bmatrix} \quad \Rightarrow \quad \mathbf{I_{\partial t}} = \frac{\partial \mathbf{I^+_{x,y}}}{\partial t} = \mathbf{D_t} * \mathbf{I^+_{x,y}} \tag{3.5}$$

Examples of this image derivatives are presented in Figure 6.13.

3.2 2D Weighted Least Square Peak Fitting Algorithm

In order to determine the lateral vibrations with the TM method I developed a 2D peak fitting algorithm to extract the sub-pixel peak position of the correlation images. The following algorithm is based on the principles of the weighted least squares Gaussian curve fitting algorithm, which itself is an extension of Caruana's fitting algorithm [11]. Building on this I extended the algorithm from 1D to 2D and I applied the principles of the algorithm to different model functions, which can be linearized. The performance of the fit is strongly dependent on the choice of a model function $f(x, y, \mathbf{p})$, whereby x and y span the 2D surface and $\mathbf{p} = \left[H, \mu_x, \mu_y, \sigma_x, \sigma_y, \theta\right]$ is the vector of fitting parameters. The 2D peaks are assumed to be oval with a height H, peak-position (μ_x, μ_y), peak-width (σ_x, σ_y) and orientation angle θ of the oval. A 2D hyperbola peak function serves as model exam-

ple in the following development of the fitting algorithm:

$$\begin{aligned} f(x,y,\mathbf{p}) &= \frac{H}{\sqrt{V+1}} \\ \text{with} \quad V &= a\left(x-\mu_x\right)^2 + 2b\left(x-\mu_x\right)\left(y-\mu_y\right) + c\left(y-\mu_y\right)^2 \\ \text{with} \quad a &= \frac{\cos(\theta)^2}{2{\sigma_x}^2} + \frac{\sin(\theta)^2}{2{\sigma_y}^2} \quad \text{and} \quad b = \frac{-\sin(2\theta)}{2{\sigma_x}^2} + \frac{\sin(2\theta)}{2{\sigma_y}^2} \\ \text{and} \quad c &= \frac{\sin(\theta)^2}{2{\sigma_x}^2} + \frac{\cos(\theta)^2}{2{\sigma_y}^2} \end{aligned} \tag{3.6}$$

In the first step the model function is linearized in order to enable solving it with the least-square approach. Therefore the linearized model function is additionally rearranged into a polynomial with the coefficients $\mathbf{p}_\alpha = \left[\alpha_0, \alpha_x, \alpha_y, \alpha_{xy}, \alpha_{x^2}, \alpha_{y^2}\right]$:

$$\begin{aligned} \frac{1}{f^2} = \frac{V+1}{H^2} &= \alpha_0 + \alpha_x \cdot x + \alpha_y \cdot y + \alpha_{xy} \cdot xy + \alpha_{x^2} \cdot x^2 + \alpha_{y^2} \cdot y^2 \\ \text{with} \quad \alpha_0 &= \frac{a{\mu_x}^2 + c{\mu_y}^2 + 2b\mu_x\mu_y + 1}{H^2} \\ \text{and} \quad \alpha_x &= \frac{-2(a\mu_x + b\mu_y)}{H^2} \quad \text{and} \quad \alpha_y = \frac{-2(c\mu_y + b\mu_x)}{H^2} \\ \text{and} \quad \alpha_{xy} &= \frac{2b}{H^2} \qquad \text{and} \qquad \alpha_{x^2} = \frac{a}{H^2} \qquad \text{and} \qquad \alpha_{y^2} = \frac{c}{H^2} \end{aligned} \tag{3.7}$$

In order to find the best fit of the data with a chosen model function the squared differences function δ^2 needs to be minimized.

$$\delta^2 = \left[\frac{1}{\hat{f}^2_{x,y}} - \left(\alpha_0 + \alpha_x x + \alpha_y y + \alpha_{xy} xy + \alpha_{x^2} x^2 + \alpha_{y^2} y^2\right)\right]^2 \tag{3.8}$$

In many cases additive random noise η in the data $\hat{f}_{x,y}$ causes huge deviations, so that the observed data follows $\hat{f} = f + \eta$ instead of $\hat{f} = f$ in the noise free case. Here f indicates an ideal distribution according to the model function. The effect is approximated with the Taylor polynomial of first order of the linearized data function:

$$\begin{aligned} \frac{1}{\hat{f}^2} = \frac{1}{(f+\eta)^2} &\approx \frac{1}{f^2} - \frac{2\eta}{f^3} \\ \Rightarrow \quad \delta &\approx \frac{1}{f^2} - \left(\alpha_0 + \alpha_x x + \alpha_y y + \alpha_{xy} xy + \alpha_{x^2} x^2 + \alpha_{y^2} y^2\right) - \frac{2\eta}{f^3} \end{aligned} \tag{3.9}$$

The revealed dependence on f of the noise effect leads to an unequal weighting of the data points, which vanishes by defining another error function

$$\epsilon = f^3\delta \approx \frac{f^3}{\hat{f}} - f^3\left(\alpha_0 + \alpha_x x + \alpha_y y + \alpha_{xy}xy + \alpha_{x^2}x^2 + \alpha_{y^2}y^2\right) - 2\eta, \tag{3.10}$$

whereby the cubed ideal distribution f^3 is multiplied to δ. This is the main principle of the weighted least square fitting method. Setting the derivatives of the sum of ϵ^2 with respect to each coefficient of $\mathbf{p}_\alpha$ to zero leads to the following linear equation system:

$$\begin{bmatrix} \sum f^6 & \sum f^6 x & \sum f^6 y & \sum f^6 xy & \sum f^6 x^2 & \sum f^6 y^2 \\ \sum f^6 x & \sum f^6 x^2 & \sum f^6 xy & \sum f^6 x^2 y & \sum f^6 x^3 & \sum f^6 xy^2 \\ \sum f^6 y & \sum f^6 xy & \sum f^6 y^2 & \sum f^6 xy^2 & \sum f^6 x^2 y & \sum f^6 y^3 \\ \sum f^6 xy & \sum f^6 x^2 y & \sum f^6 xy^2 & \sum f^6 x^2 y^2 & \sum f^6 x^3 y & \sum f^6 xy^3 \\ \sum f^6 x^2 & \sum f^6 x^3 & \sum f^6 x^2 y & \sum f^6 x^3 y & \sum f^6 x^4 & \sum f^6 x^2 y^2 \\ \sum f^6 y^2 & \sum f^6 xy^2 & \sum f^6 y^3 & \sum f^6 xy^3 & \sum f^6 x^2 y^2 & \sum f^6 y^4 \end{bmatrix} \begin{bmatrix} \alpha_0 \\ \alpha_x \\ \alpha_y \\ \alpha_{xy} \\ \alpha_{x^2} \\ \alpha_{y^2} \end{bmatrix} = \begin{bmatrix} \sum f^6 \hat{f}^{-2} \\ \sum f^6 x \hat{f}^{-2} \\ \sum f^6 y \hat{f}^{-2} \\ \sum f^6 xy \hat{f}^{-2} \\ \sum f^6 x^2 \hat{f}^{-2} \\ \sum f^6 y^2 \hat{f}^{-2} \end{bmatrix}$$

$$\mathbf{A} \cdot \mathbf{p}_\alpha = \mathbf{b} \quad \Leftrightarrow \quad \mathbf{p}_\alpha = \mathbf{A}^{-1} \cdot \mathbf{b} \tag{3.11}$$

which can be solved for the parameters $mathbf p_\alpha$ by multiplying with the matrix inverse of $\mathbf{A}$. The omitted higher terms of the Taylor expansion of the noise can noticeably affect the fit, if the data shows the peak with a long tail. And additionally, the ideal values for f are unknown so the noisy data values $\hat{f}$ are used. Therefore an iterative algorithm is introduced using Equation 3.11, whereby every iteration adjusts the weighting until it converges:

$$f_{(k)} = \left\{ \begin{array}{c} \hat{f} \quad \text{for} \quad k = 0 \\ \left(\alpha_{0,(k)} + \alpha_{x,(k)} x + \alpha_{y,(k)} y + \alpha_{xy,(k)} xy + \alpha_{x^2,(k)} x^2 + \alpha_{y^2,(k)} y^2\right)^{-\frac{1}{2}} \quad \text{for} \quad k > 0 \end{array} \right\} \tag{3.12}$$

the parameters $\mathbf{p}$, which contain the sub-pixel peak position of the correlation images are calculated from the resultant coefficients $\mathbf{p}_\alpha$ according to Equation 3.7 and Equation 3.6.

Chapter 4

Optical Flow Algorithms

4.1 Lucas-Kanade Algorithm

The aim of the Lucas-Kanade algorithm is to provide an estimate of motion for interesting features in successive frames of a scene. Therefore it uses the image derivatives $\mathbf{I}_{\partial \mathbf{x}}$, $\mathbf{I}_{\partial \mathbf{y}}$ and $\mathbf{I}_{\partial \mathbf{t}}$ to calculate the motion vector $\mathbf{\Delta x} = (u, v)$ at certain 'points of interest' [12]. The following two assumptions are done by the algorithm:

4.1.1 Assumptions

- The movement of objects between two successive frames is small. The algorithm works best for sub-pixel movement, which should not be to small neither.
- The frames should show natural scenes with smoothly changing intensity levels.

4.1.2 Functional Principle

When looking at one pixel with a certain intensity value j, the spatial derivatives, which are determined as describe in section 3.1, indicate the direction of increasing brightness in x- and y-direction. A higher intensity value k of the successive frame at the same pixel results in a positive value for the temporal derivative, and one can assume that the movement occurred against the direction of increasing brightness, since a higher brightness moved into the observed pixel (see example in Figure 4.1). This works vice versa for a lower succeeding intensity. The change in intensity $\mathbf{\Delta I}_{\mathbf{x,y,t}}(u, v)$ at the pixel (x, y) due to a movement (u, v) is calculated in Equation 4.1 using the spatial derivatives. The change in intensity over a pixel displacement (u, v) equals the negative temporal derivative, since

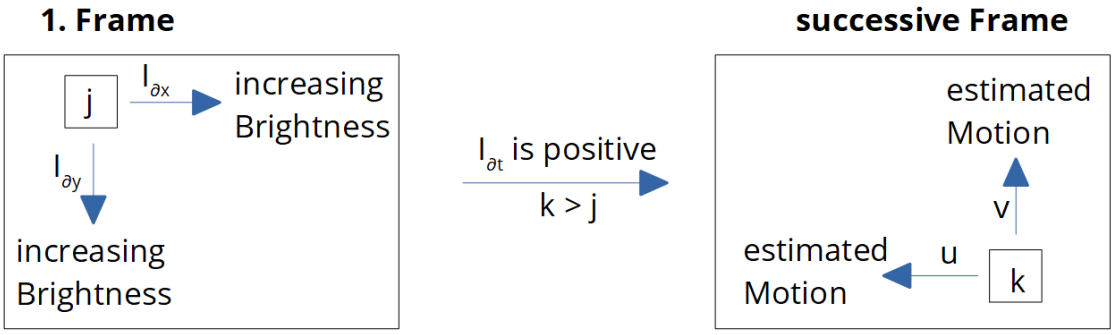

Figure 4.1: Technique of Lucas-Kanade algorithm. The spatial derivatives determine the direction of increasing brightness. Comparing this with the temporal derivative leads to the estimated motion.

the object moves over time rather than the observing pixel.

$$\mathbf{\Delta I_{x,y,t}}(u,v) = \mathbf{I_{\partial x}}(x,y,t) \cdot u + \mathbf{I_{\partial y}}(x,y,t) \cdot v = -\mathbf{I_{\partial t}}(x,y,t) \tag{4.1}$$

This provides one equation with two unknowns without a unique solution. Assuming smooth spatial changes of the movement enables considerations of the 3×3 pixel neighborhood, thus adding eight equations and creating an overdetermined equation system:

$$\begin{aligned} &\mathbf{I_{\partial x}}(x+\Delta x, y+\Delta y, t) \cdot u + \mathbf{I_{\partial y}}(x+\Delta x, y+\Delta y, t) \cdot v = -\mathbf{I_{\partial t}}(x+\Delta x, y+\Delta y, t) \\ &for \quad \Delta x = -1,0,1 \quad and \quad \Delta y = -1,0,1 \end{aligned} \tag{4.2}$$

Summarized as:

$$\mathbf{S} \cdot \begin{pmatrix} u \\ v \end{pmatrix} = \vec{t} \tag{4.3}$$

where the vector $\vec{t}$ contains the 9 terms $-\mathbf{I_{\partial t}}(x+\Delta x, y+\Delta y, t)$ and the 9×2 matrix $\mathbf{S}$ consists out of the rows $\left(\mathbf{I_{\partial x}}(x+\Delta x, y+\Delta y, t), \mathbf{I_{\partial y}}(x+\Delta x, y+\Delta y, t)\right)$. The least squares solution is found by multiplying the equation by S^T.

$$\mathbf{S^T S} \begin{pmatrix} u \\ v \end{pmatrix} = \mathbf{S^T \tilde{t}} \quad \Leftrightarrow \quad \begin{pmatrix} u \\ v \end{pmatrix} = \left(\mathbf{S^T S}\right)^{-1} \mathbf{S^T \tilde{t}} \tag{4.4}$$

4.1.3 Points of Interest

The Least Squares solution is only appropriate, if $\mathbf{S^T S}$ is invertible. Therefore, none of the two eigenvalues λ_1 and λ_2 are supposed to be zero. If the eigenvalues are small

the solution can still be ill-conditioned. This leads to the following criteria for points of interest:

- A pixel is called point of interest only if both eigenvalues of $\mathbf{S}^{\mathrm{T}}\mathbf{S}$ are large, which is measured by a adjustable threshold. Two large eigenvalues indicate the large intensity gradients in two nearly orthogonal directions. Interestingly this correspond directly to the criteria of corners in an image developed by Harris et al. [13].

4.2 Optical Flow Estimation for a Periodic Image Sequence

The general idea of OFEPIS [14] is that the intensity I_t at position (x, y) equals the intensity I_{t+1} of the successive frame at position $(x + u, y + v)$, whereby (u, v) is the displacement vector in between the two frames, thus:

$$I(x + u, y + v, t + 1) = I(x, y, t) \tag{4.5}$$

4.2.1 Harmonic Model Approach

Since a harmonic oscillation is induced by the actuator, the responding motion of the sample is assumed to harmonically oscillate with the same frequency as well. This leads to the following approach for the displacement vector (u, v):

$$\begin{aligned} u(x, y, t) &= \sum_{l=1}^{L} a_l(x, y) \cdot \cos(\omega_l t) + b_l(x, y) \cdot \sin(\omega_l t) \\ v(x, y, t) &= \sum_{l=1}^{L} c_l(x, y) \cdot \cos(\omega_l t) + d_l(x, y) \cdot \sin(\omega_l t) \\ with \quad \omega_l &= \frac{2\pi l}{T}, \end{aligned} \tag{4.6}$$

whereby L indicates the harmonic order of the periodic approach and T the number of frames of the periodic image sequence.

4.2.2 Optimization Criteria

As optimization criterion the algorithm aims to minimize the deviation of the equality in Equation 4.5 over the whole image domain D, which is given by:

$$E_1(u, v) = \sum_{t=0}^{T-1} \int_D \left(I(x, y, t) - I(x + u, y + v, t + 1)\right)^2 dxdy \tag{4.7}$$

Additionally, a spatial smoothness term is introduced as second criterion in order to minimize the deviation in the movement of neighboring pixels:

$$E_2(u,v) = \sum_{t=0}^{T-1} \int_D \left(|\nabla u|^2 + |\nabla v|^2 \right) dxdy \tag{4.8}$$

These two optimization criteria are summed to the following energy function, which is to be minimized. α is the weighting parameter between the two constraints.

$$E(u,v) = E_1(u,v) + \alpha E_2(u,v) \tag{4.9}$$

Now $I(x+u, y+v, t+1)$ can be approximated by its Taylor expansion to the first order, since the first order image derivatives are already known from section 3.1.

$$I(x+u, y+v, t+1) \approx I(x,y,t) + \frac{\partial I}{\partial x}u + \frac{\partial I}{\partial y}v + \frac{\partial I}{\partial t} \tag{4.10}$$

Inserting Equation 4.10 into Equation 4.7 leads to the following expression:

$$E_1(u,v) = \sum_{t=0}^{T-1} \int_D \left(\frac{\partial I}{\partial x}u + \frac{\partial I}{\partial y}v + \frac{\partial I}{\partial t} \right)^2 dxdy \tag{4.11}$$

Replacing u and v by their approaches in Equation 4.6 results in

$$E_1(u,v) = \sum_{t=0}^{T-1} \int_D \left(\sum_{l=1}^{L} \left(I_{a_l} a_l + I_{b_l} b_l + I_{c_l} c_l + I_{d_l} d_l \right) + I_t \right)^2 dxdy \tag{4.12}$$

whereby $I_{a_l} = {}^{\partial I}/_{\partial x} \cdot \cos(\omega_l t)$ and $I_{b_l} = {}^{\partial I}/_{\partial x} \cdot \sin(\omega_l t)$ and $I_{c_l} = {}^{\partial I}/_{\partial y} \cdot \cos(\omega_l t)$ and $I_{d_l} = {}^{\partial I}/_{\partial y} \cdot \sin(\omega_l t)$. Equation 4.5 is substituted also into Equation 4.8 which results in:

$$E_2 = \frac{T}{2} \sum_{l=1}^{L} \int_D \left(|\nabla a_l|^2 + |\nabla b_l|^2 + |\nabla c_l|^2 + |\nabla d_l|^2 \right) dxdy \tag{4.13}$$

Since the optimization criterion from Equation 4.9 depends on $4 \cdot L \cdot X \cdot Y$ unknown variables it needs to be solved numerical using the iterative Jacobi method[1]. The iterative algorithm [14] is implemented in the analysis software described in section 6.3.

[1]Further information about this method are given in source [15]

Chapter 5

Evaluation Measurement Setup

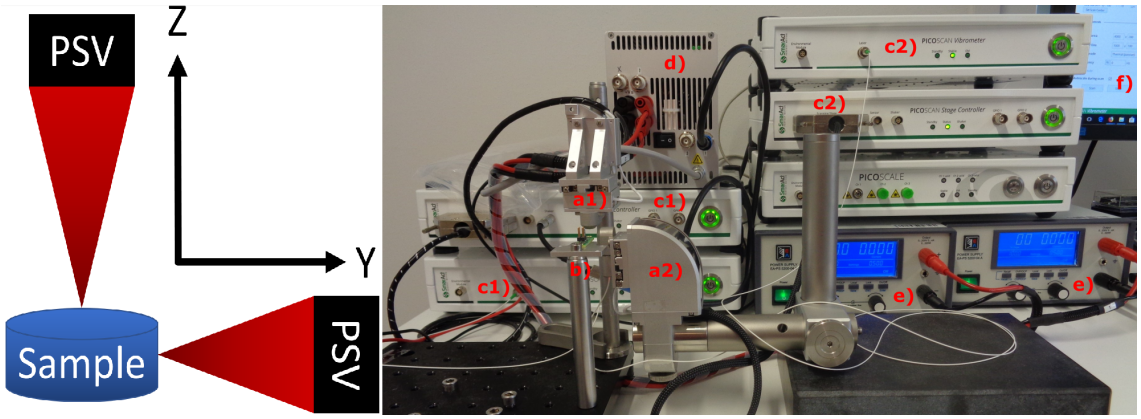

Figure 5.1: Measurement setup for quantification of the developed method to determine lateral vibrations. Two PSVs measure the lateral vibrations from above and aside. a) Scanning stages b) Sample holder with sample c) Each vibrometer consists out of an interferometer unit and a stage controller d) Amplifier operates on the actuating signal e) Power supplies for amplifier f) Computer with vibrometer user interface.

In order to obtain the 3D vibration behavior, it is necessary to measure out-of-plane vibrations as well as in-plane vibrations. The PSV is a scanning interferometer which was conventionally developed to record out-of-plane vibrations. Using two conventional PSVs, which image the sample from tow orthogonal sides, enables recording of 3D vibration (see Figure 5.1). The results of these reference measurements are then used to verify the results from the developed in-plane measurement routine. If this routine can be validated a 3D vibration measurement can be performed using only one PSV. Here the two PSVs are simultaneously used to record the amplitude and phase of their respective out-of-plane vibration (usual function of the instrument) and additionally provide phase related intensity data, which can later be processed to extract lateral vibrations. The scan-

ning stages of the vibrometers and a sample holder are mounted on a breadboard or a granite block and they are adjusted in a way that the sample lies within both scanning volumes. A power amplifier was used in some experiments to enable higher amplitudes of the output voltage signal in order to induce larger vibrations. The samples are either excited directly, if they include their own actuation mechanism (e.g. loudspeakers or MEMS microgrippers), or they are mounted on an external piezo actuator (e.g. cantilevers).

5.1 PICOSCAN Vibrometer

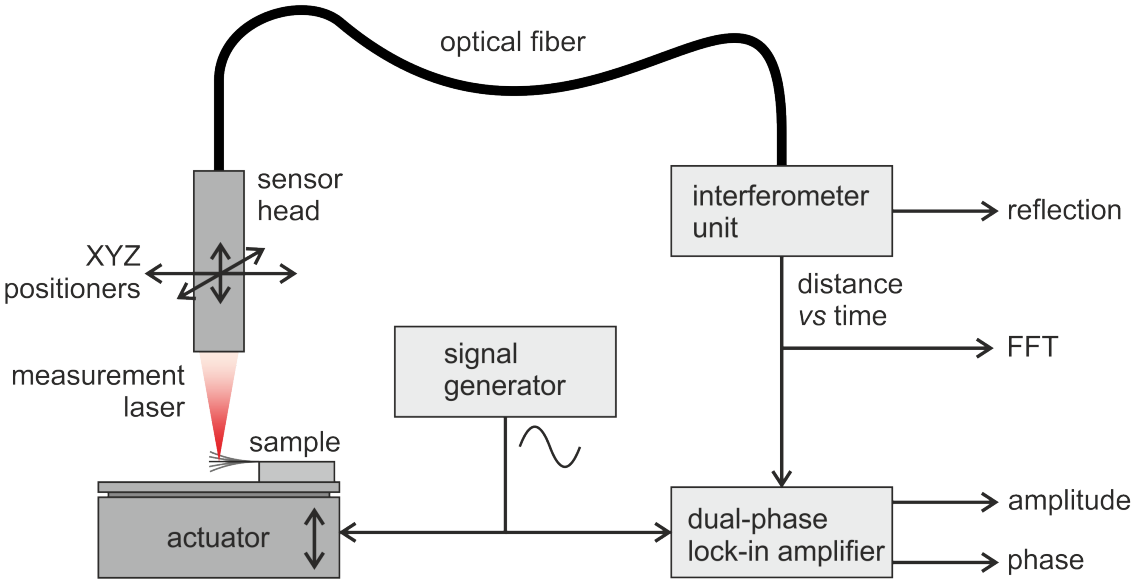

Figure 5.2: Schematic of PSV. The sensor head of a Michelson interferometer is mounted to a x,y,z scanning stage. Additionally a signal generator actuates the sample and simultaneously provides the reference signal for the dual-phase LIA, which extracts amplitude and phase of the vibration from the position signal.

The PSV developed by SmarAct GmbH is based on SPM interferometry using a Michelson setup realized with optical fibers (theory described in section 2.2). The confocal interferometer head is able to focus the infrared laser ($\lambda = 1550\,\text{nm}$) to a 7 µm Gaussian spot and it is mounted onto a 3D positioning stage (x,y,z), which enables scanning of the sample and adjustment of focus. Due to the implemented confocal optics a lateral resolution of down to 5 µm is reached. In confocal microscopy the sample is raster-scanned and the light intensity at each pixel is recorded. The confocal principle ensures that only light that originates from the focus is recorded while all out-of-focus light is suppressed. Such a confocal scanning microscope is implemented in the PSV with optical fibers [16].

The positioners are based on an unique piezo stick-slip stepping motion[1], which is developed by SmarAct GmbH. The integrated function generator, which is based on a 12 bit direct digital synthesizer (DDS),[2] provides a sinusoidal signal to actuate the sample, which could either have its own actuation mechanism or it is actuated by a mechanical actuator stage. This actuating signal serves as reference for the dual-phase LIA[3] (based on a field programmable gate array (FPGA)), which is able to extract the amplitude and relative phase from the interferometer position signal at the reference frequency. More detailed specifications of the PSV are provided in Appendix 8.5.

5.1.1 Measurement Procedure for Out-of-Plane Vibrations with the PSV

1. At first the wavelength modulation and the gains of the SPM interferometer need to be adjusted, so that the quadrature signal (see Figure 2.5) appears as a circle. The adjustment needs to be done on the sample surface at a position that shows a high reflection of the infrared laser.

2. A confocal microscopy image of the sample is recorded in order to get an overview of the sample structure.

3. The measurement head is positioned at a selected point of interest on the sample and the position signal is recorded while the signal generator actuates the sample with a frequency sweep. A fast Fourier transform (FFT) of the position signal reveals the dynamic response of the observed feature of the sample, whereby peaks usually correspond to resonance modes at respective eigenfrequencies.

4. The sample is actuated at a selected frequency of interest (from the FFT) while the measurement head scans the amplitude and phase of the actuated frequency component in the position signal using the LIA. This information is used to construct 3D deflection images of the sample surface at the selected frequency.

[1] Further information at `http://www.smaract.com/technology/` (03.10.2018)
[2] Information about DDS found in source [17].
[3] Further information about lock-in amplifiers are given in source [18]

5.2 Piezo Based Actuator Stage

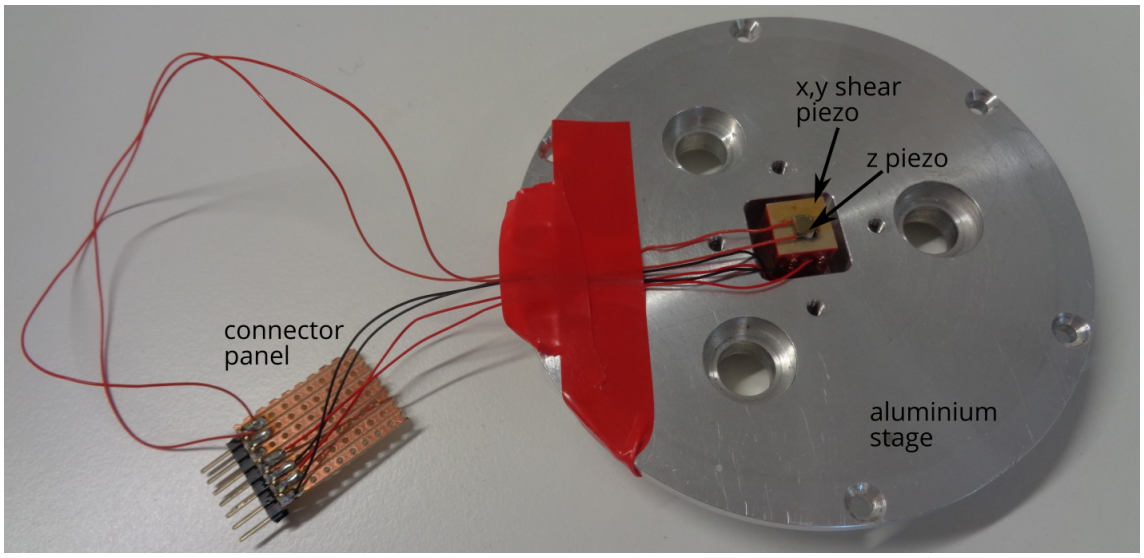

Figure 5.3: Piezo based actuator stage to excite samples externally.

For those experiments whereby cantilevers are observed, the P-142.05 shear piezo from Physik Instrumente (PI) [19] is used as actuator stage, since the cantilevers do not have a mechanism to be actuated directly. A piezo chip PA3JE from Thorlabs [20], which is able to oscillate in z-direction, is placed on top of the shear piezo, which offers actuation in x-,y-direction. Thus, the complete actuator stage offers actuation in all three dimensions. However, in these experiments only the y-direction of the shear piezo. was excited.

5.3 Samples

In order to test the post processing algorithms to reveal lateral vibrations I investigated two different samples made of silicon, which have micrometer sized structures to investigate:

- The delta-shaped cantilever F from the Bruker MLCT-O10 cantilevers chip [21] (see Figure 5.4). This sample is actuated externally by the actuator stage.
- The left gripper arm of the Femtotools FT-G60 Microgripper (FT-G60), which can be actuated electrostatically using its comb structure. (see Figure 5.5 and Appendix 8.5).

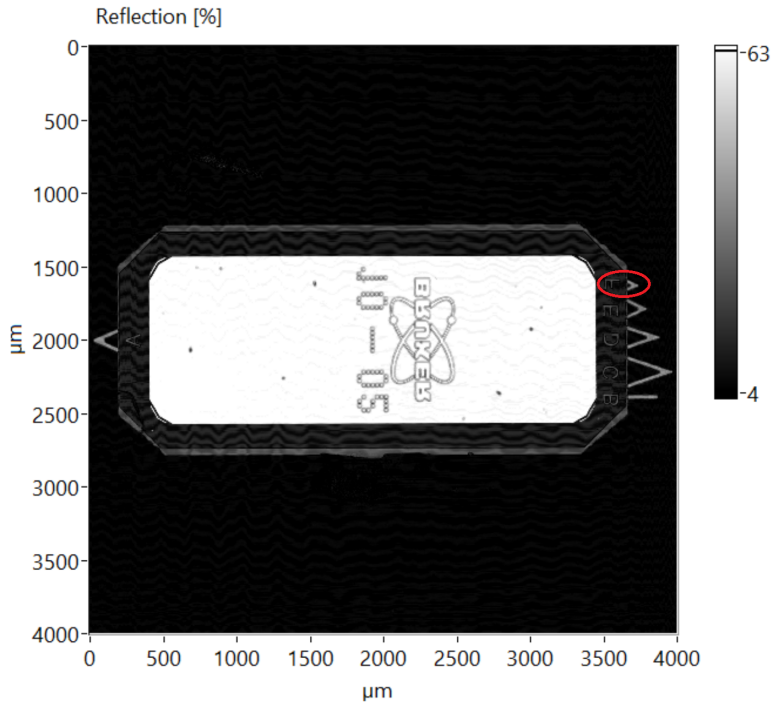

Figure 5.4: Confocal microscopy image of the Bruker MLCT-O10 cantilevers with one megapixel resolution. Scanning area: 4mm x 4mm. Cantilever F within red region.

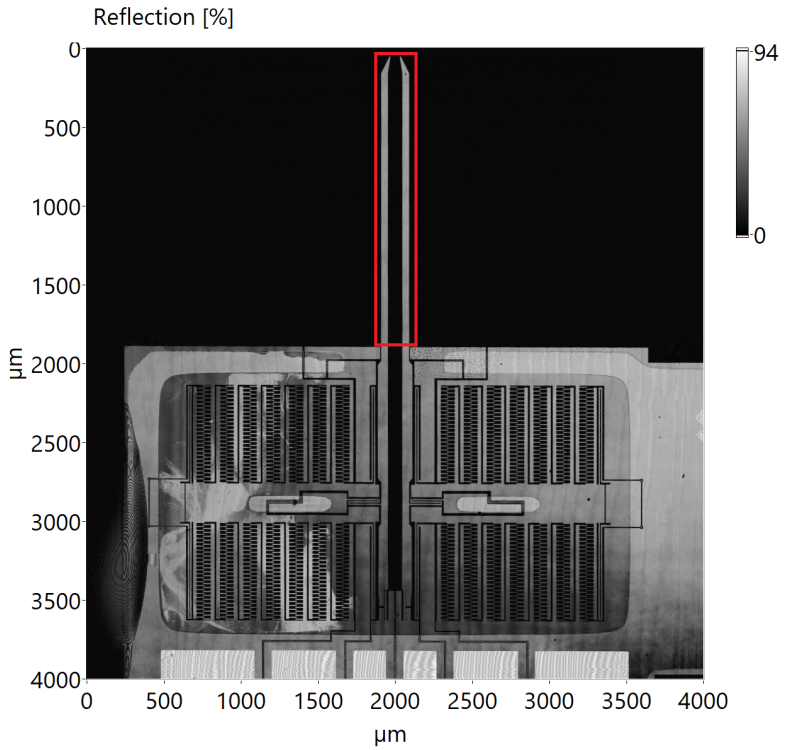

Figure 5.5: Confocal microscopy image of the Femtotools FT-G60 microgripper with one megapixel resolution. Scanning area: 4mm x 4mm. The red region indicates the scanning area, which is recorded by the PSV. The total length of one microgripper arm is about $L \approx 2847\,\mu m$, determined by this microscopy image. However only about 1650 µm are recorded within the red scanning area.

Chapter 6

In-Plane Vibration Analysis

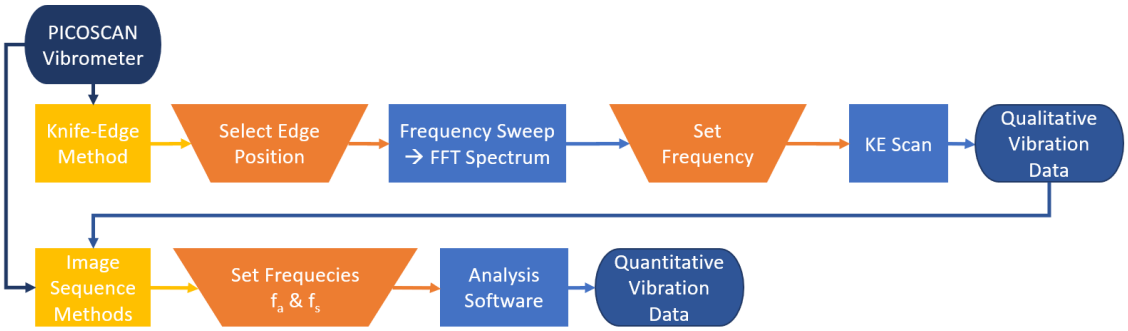

Figure 6.1: Operating workflow to investigate lateral vibrations using the PSV. The initialization of the instrument is the same for out-of-plane vibrations. The knife-edge method gives qualitative information about interesting frequencies and features. The image sequence methods enable quantitative investigation of the vibrational motion of selected features at chosen frequencies.

Two main ideas gave the basic foundation for the development and implementation of the following workflow in Figure 6.1 to investigate in-plane vibrations using the PSV. The knife edging (KE) [22], further described in section 6.1, uses the oscillating intensity signal measured on an preferably sharp intensity edge, which vibrates perpendicular to its edge orientation. The PSV can process this intensity signal either by calculation of an FFT or by filtering with its LIA in order to extract frequency related vibration information. In the second approach to reveal in-plane vibrations an image sequence of the vibrating sample is constructed using intensity and phase data from the PSV (see subsection 6.3.1). There are various optical flow algorithms to estimate the motion of this image sequence by post processing. Here the mainly used optical flow method revealing in-plane vibrations is TM (described in subsection 6.3.3), whereby algorithms of the single TM-steps are developed and implemented into an analysis software. Two other motion estimation algorithms

were implemented and applied in order to compare to the TM-method. It turned out that using the KE-method with the PSV does not offer quantitative investigation of in-plane vibrations, however it still serves as a qualitative measure capable of revealing which feature vibrates at which frequency. Hereby the much shorter measurement time and no need of post processing are the advantages of performing KE before the time consuming measurements to construct image sequences, which then provide quantitative information about the vibrational motion of the sample.

6.1 Knife Edging

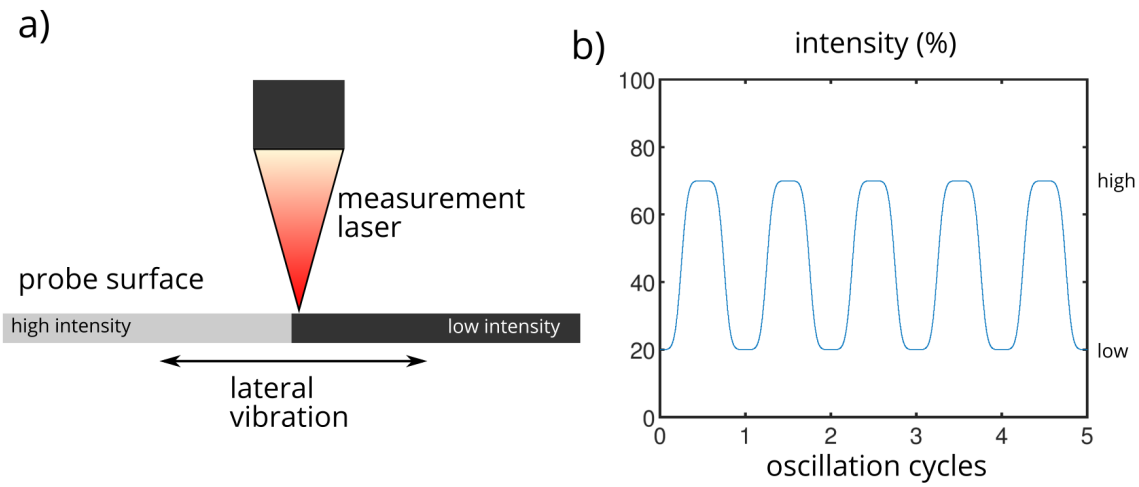

Figure 6.2: Knife-Edge principle. a) Scheme on vibrating edge between two regions of different intensity (Low: 20% reflection, High: 70% reflection). The measurement laser is focused on a spot near the edge. b) The graph shows the recorded intensity over the oscillation cycles of the sample.

The KE-method is performed before quantitative vibration measurements in order to get a qualitative indicator of the vibrating features and their resonance frequencies [23]. As seen in Figure 6.2 a) the measurement laser is focused onto an edge of the sample structure, which separates two regions of different reflection intensity. The edge oscillates together with the whole sample so that the measurement laser detects the different intensities of the two regions alternatively. This results in the oscillating intensity signal seen in Figure 6.2 b). Each rising and falling flank of the signal follows the shape of the antiderivative of a Gaussian. This results from the approximately Gaussian beam profile of the laser described by $G(x)$, whereby $x_0 = 0$ is set to be in the center of the Gaussian laser spot and σ is a measure of its width, since it relates to the full width at half maximum

(FWHM) as $FWHM = 2\sqrt{2\ln(2)}\sigma$ [24].

$$G(x) = \frac{1}{\sigma\sqrt{2\pi}} \cdot e^{\frac{-x^2}{2\sigma^2}} \tag{6.1}$$

KE can only reveal the vibration components which are orthogonal to the edge orientation, since no intensity variation can be observed while the sample moves parallel to the investigated edge. Therefore, corner points are interesting in order to reveal vibrations in all directions. In general the edge of the sample oscillates at the actuated frequency f_a with an amplitude $A_\perp$ (only the component, which is perpendicular to the edge) around its rest position d, which is the distance of the edge to the center of the laser spot. The phase offset φ_0 is given by the relative phase shift between the edge oscillation and the actuating signal.

$$x_{edge}(t) = A_\perp \cdot \cos(2\pi f_a \cdot t + \varphi_0) + d \tag{6.2}$$

An important assumption of this method is, that the edge separates two regions of different reflection intensity I, whereby each region has a constant intensity. The portion of the Gaussian laser beam, which hits the region with the higher intensity can be determined by the integral from negative infinity to the x-position of the edge. This and the respective integral of the low reflection region are each multiplied by their intensity values I_{High} and I_{Low} and summed up to result in the total intensity measured, which is dependent on the position of the edge.

$$I(x_{edge}) = I_{High} \cdot \int_{-\infty}^{x_{edge}} G(x)dx + I_{Low} \cdot \int_{x_{edge}}^{\infty} G(x)dx \tag{6.3}$$

This equation can be rewritten by inserting Equation 6.2 into Equation 6.3:

$$I(t) = \frac{I_{High} - I_{Low}}{2} \cdot erf\left(\frac{A_\perp \cdot \cos(2\pi f_a \cdot t + \varphi_0) + d}{\sigma\sqrt{2}}\right) + \frac{I_{High} + I_{Low}}{2} \tag{6.4}$$

For $A_\perp \ll \sigma$ and $d \ll \sigma$ this function can be approximated by its Taylor expansion up to the first order resulting in a purely sinusoidal signal oscillating at the actuating frequency.

$$I(t) \approx \bar{I} + \Delta I \cdot \frac{A_\perp \cos(2\pi f_a \cdot t) + d}{\sigma\sqrt{2\pi}} \quad \text{with} \quad \bar{I} = \frac{I_{High} + I_{Low}}{2} \quad \text{and} \quad \Delta I = I_{High} - I_{Low} \tag{6.5}$$

However if $A_\perp > \sigma$ and $d > \sigma$, the harmonics of the actuating frequency f_a appear, which can be shown by the Fourier transformation of the intensity signal (derivation found in

Appendix 8.5):

$$\mathfrak{F}^{+}\{I(t)\}(\omega) = 4\Delta I\sqrt{\pi}\sum_{k=0}^{\infty}\frac{(-1)^k(2k)!}{k!}\sum_{l=1}^{1+2k}\frac{\left(\frac{\sqrt{2}A_{\perp}}{4\sigma}\right)^l d^{1+2k-l}}{(1+2k-l)!}\sum_{m=1}^{l}\frac{s_e(l+m)}{\left(\frac{l-m}{2}\right)!\left(\frac{l+m}{2}\right)!}\delta(m\omega_a-\omega) \tag{6.6}$$

The harmonics, which are indicated by the term $\delta(m\omega_a - \omega)$, overlay the actual frequency response of the lateral vibrations and should not be mistakenly interpreted as resonance modes (an example found in Figure 6.3). However generally the amplitudes of these oscillating intensity signals can be extracted with either the FFT-calculation or the lock-in filtering offered by the PSV. Although higher amplitudes in the measured intensity signal indicate larger vibration amplitudes, quantitative investigation using KE is difficult due to many reasons, which also influence the amplitude of the oscillating intensity:

- The high and low reflectance I_{High} and I_{Low} of the two regions, which are separated by the edge. The reflectance of the two regions may not be uniform.
- The relative angle of the vibration direction towards the edge orientation. Only orthogonal components are measured.
- The relative position distance d of the center of the laser spot to the edge. It is difficult to exactly position the laser on the edge.
- The width σ of the Gaussian laser spot. The shape and the width are approximations.
- The dependence of the unknown vibration amplitude on the measured intensity amplitude is nonlinear.

All this reasons promote using the KE-technique rather qualitatively, because for quantitative investigation all these influences need to be determined and taken into account. Additionally, it seemed to be easier to extract quantitative vibration information with the image sequence methods. Therefore KE is used to reveal the features and frequencies which show vibrational resonances, to prepare the measurement of an periodic image sequence.

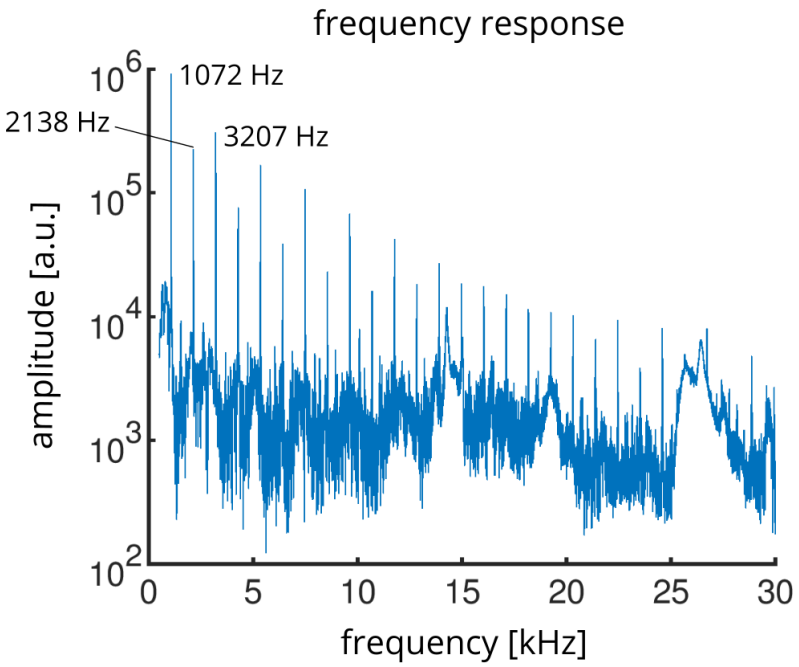

Figure 6.3: Frequency response of intensity using the KE-principle. A piezo driven laser scanner was driven with a frequency sweep from 500 Hz to 30 kHz, which reveals a sharp resonance peak at 1072 Hz. The spectrum shows many harmonics which decrease slowly in amplitude.

6.1.1 Dynamic Response via FFT using Knife Edging

The KE-method can be used to determine a qualitative dynamic response of the sample revealing the frequencies of in-plane resonances, which can be investigated in more detail with the KE-scan or the analysis software (described in section 6.3). The user can position the measurement head of the PSV above an edge of a feature of interest in the former recorded microscopy image. The intensity signal is recorded while the sample is actuated with a frequency sweep, which range is also set by the user. The PSV directly calculates the FFT of the intensity signal. Since the sinusoidal approximation of the signal in Equation 6.5 only holds for small amplitudes, since large vibrations add harmonics of the actuating frequency to the spectrum of the intensity signal. These artifacts in the frequency spectrum could hide the actual information of the affected frequencies. Figure 6.3 shows a measured dynamic response of a piezo driven laser scanner, whereby the lateral vibration amplitude is larger than the spot size so that harmonics of the ground frequency appear.

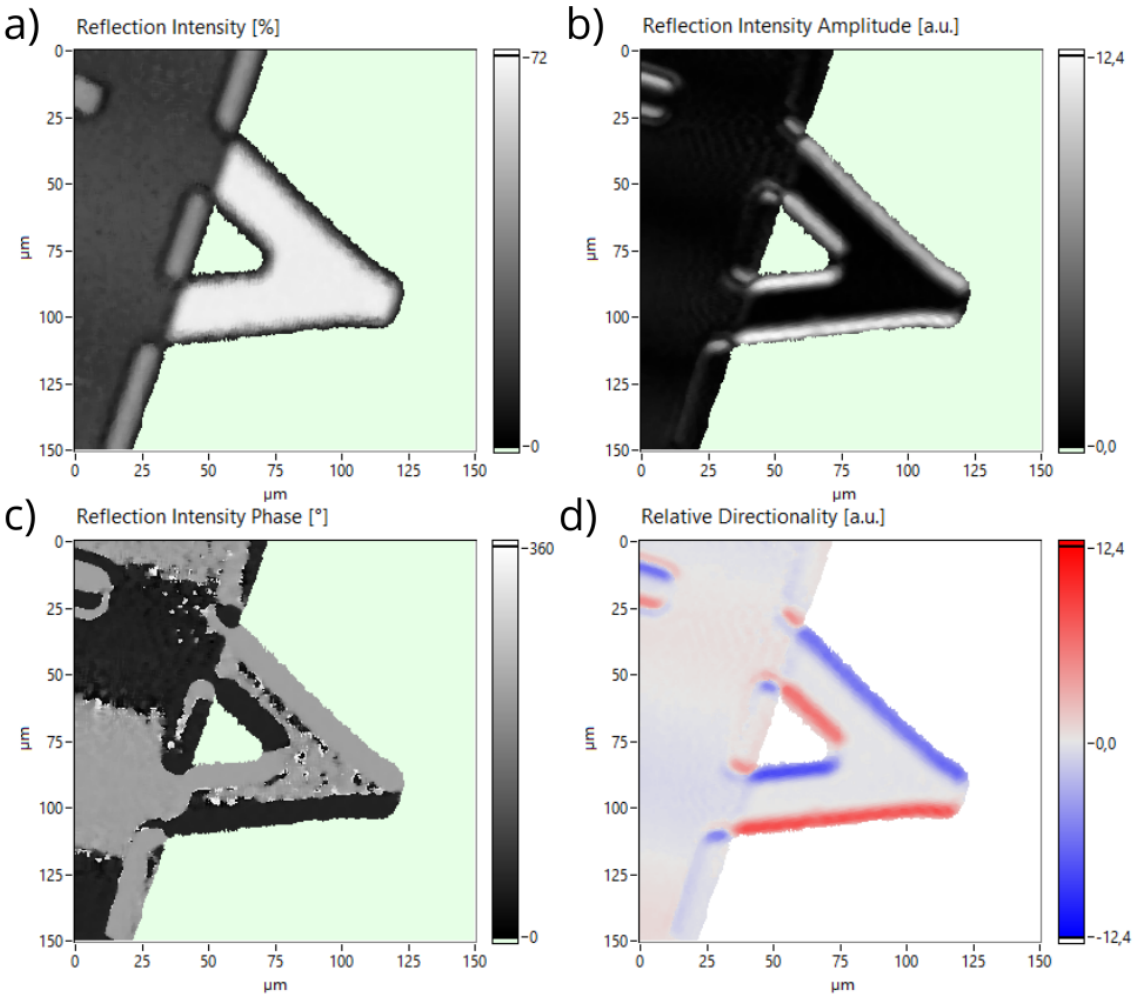

Figure 6.4: KE-scan of the delta shaped Bruker cantilever at 1072 Hz a) Confocal microscopy image with 0.5 µm scanning-resolution b) Amplitude of reflection intensity filtered using a LIA c) Phase of the reflection intensity signal filtered using a LIA d) Deflection image combining amplitude and phase data, which reveals an estimate of the direction of vibration (The vibration direction roughly follows the direction of the chip edge on which the cantilever is mounted).

6.1.2 Scan at Resonance

The knife-edge method can also be used in scanning mode at chosen frequencies to unveil moving features and to give a qualitative estimate of the motion's direction. For each pixel position it records the intensity signal in order to detect whether there is a moving edge. It then filters this intensity signal using a dual phase LIA in order to extract amplitude and phase of the reference frequency component. Combing the KE-information of all image pixels offers a qualitative measure of the vibration direction assuming that a feature moves uniformly and is surrounded by multiple edges (e.g. like the cantilever in Figure 6.4). Edges which have the same orientation but opposite intensity gradients show

a 180° relative phase shift (blue verses red). If the scanning resolution is smaller than the laser spot diameter also the thickness of edges with large amplitudes can be interpreted as an estimate of the amplitude of the lateral oscillation.

6.2 Recording Phase Related Intensity Data using the PSV

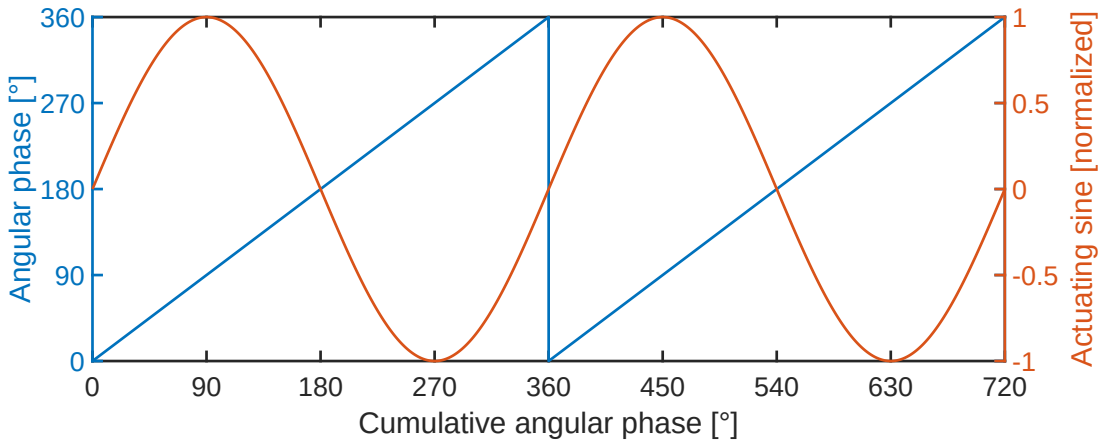

Figure 6.5: Synchronized output signals of the PSV signal generator. The red sine wave actuates the sample to be investigated. The blue sawtooth signal outputs the momentary angular phase of the actuating signal in degrees.

In order to create a periodic image sequence of the moving sample it is necessary to have intensity frames for T equally distributed angular phases of the actuating sinusoidal signal. The PSV cannot capture wide-field images directly (recording multiple pixels simultaneously), it rather raster-scans the sample surface, whereby its measurement head stops at each pixel to record position and intensity. Hereby the PSV offers recording multiple data sets at each position. The measured intensity values at two different pixels are not necessarily recorded at the same angular phases, because the data recording cannot be triggered on the actuation signal. Therefore, the amount N of data sets recorded at each pixel is chosen to be much higher than the number of frames ($N \gg T$) and necessarily the momentary angular phase of each of the N intensity values at each pixel must be recorded additionally. The frames can be constructed from this randomly over-sampled data during post processing using different methods described in subsection 6.3.1. In contrast to the intensity the PSV does not provide the option to directly record the momentary angular phase of the actuation signal, which is generated by a DDS[1]. This issue is

[1]Further information about DDS in source [17]

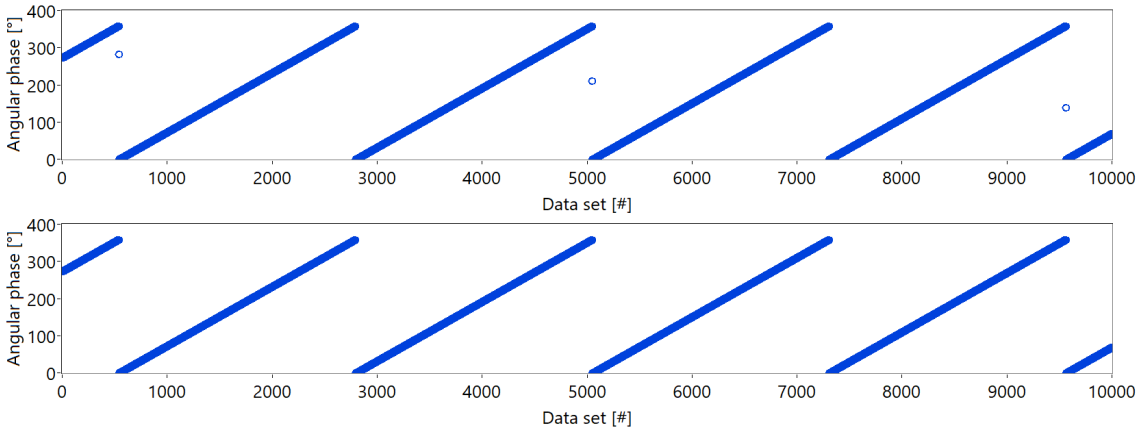

Figure 6.6: Angular phases at which the PSV recorded data sets a) The first, third and fifth falling edge show wrongly recorded angular phases due to the interpolation of the DDS in between the largest and smallest value. b) Shows the corrected angular phase data without artifacts.

solved by adding a second DDS-based signal generator providing a sawtooth signal, which is synchronized to the actuating signal having the same frequency (see Figure 6.5). The DDS of the PSV has a 12 bit resolution leading to 4096 entries in its look-up table, which are equally distributed in the interval $[0°, {}^{4095}/_{4096} \cdot 360° \approx 359.912°]$. The resolution is increased by linearly interpolating in between these entries. Unfortunately this leads also to an unwanted interpolation between the largest value and zero, which is observed as falling edges in Figure 6.6 and which maps the actual phase values within the interval $[359.912°, 360°]$ proportionally into the interval $[359.912°, 0°]$. Using this information allows correction of these wrongly measured phase values during post processing in the analysis software according to the formula:

$$\varphi_{cor} = \left[4095 + \left(1 - \varphi_{err} \cdot \frac{4096}{4095 \cdot 360}\right)\right] \frac{360}{4096} = 360 - \frac{\varphi_{err}}{4095} \tag{6.7}$$

6.2.1 Choice of Sampling Frequency

The reflection and angular phase at each pixel are recorded with the sampling frequency f_s, which needs to be adjusted according to the actuated frequency f_a and the number of recorded data sets N at one pixel. The aim is to measure the reflection at one pixel for N different equal distributed angular phases of the actuated sine. As discussed before this is necessary, because synchronizing the offset phase of the data recording at each pixel

is not offered by the PSV yet. The frequencies f_a and f_s are stated in Hertz and can adopt only integer values. A simple solution for low actuated frequencies f_a is given as:

$$f_{s,low} = N \cdot f_{a,low} \tag{6.8}$$

whereby the N data pairs are distributed over one period of the actuated sine. However f_s is limited to 5 MHz, N should be large (e.g. 1000 - 10000), since it leads to a small maximal angular phase error of the built image frames and f_a can be chosen in a wide range (500 Hz - 2.5 MHz). This disables the solution in Equation 6.8 for large f_a. In addition, sampling over multiple periods enables averaging, so that measurement outliers have less influence on the results. Therefore, I suggest another method with the following criteria:

- The N samples are distributed equally over an integer number of periods P, which are at least two and at most $N-1$. By subtracting or adding multiples of 2π all angular phases are mapped into one period given by the interval $[0; 2\pi]$.
- The maximal distance between two angular phases recorded should be minimized.

The first criterion leads to Equation 6.9, which gives $N-2$ possible sampling frequencies.

$$f_s = f_a \cdot \frac{N}{P} \quad with \quad 2 \leq P \leq N-1 \tag{6.9}$$

The second criterion helps to determine the best choice by minimizing the maximal distance between two measured angular phases. A lot of bad choices can be filtered out by the following criterion:

- N and P should not have any common divisor except one.

If the greatest common divisor $g = gcd(N, P)$ is greater than one, g measured samples are mapped to the same angular phase in the interval $[0; 2\pi]$, which increases the maximal distance between two different measured angular phases by a factor of g. If N samples are measured over P periods than N/g samples are measured over P/g periods, which just happens g times equally, whereby all information lies already in this first N/g samples and P/g periods. Therefore g needs to be one in order not to lose accuracy. In theory all remaining factors N/P with $g = 1$ have the best accuracy achievable with N points. But since f_s is rounded to the next integer another phase error occurs, which depends on how close f_s is to the next integer. The best choice is determined by calculating

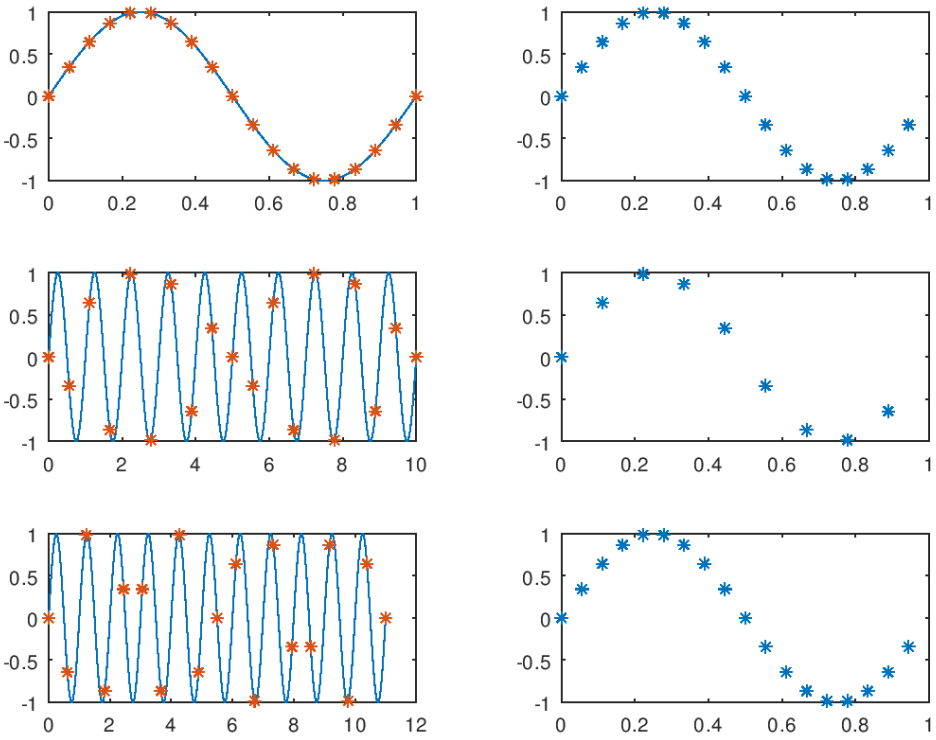

Figure 6.7: Comparison of sampling frequency factors. The left plots show $N = 18$ samples equally distributed over different numbers of periods (1,10,11). The right plots display the mapped angular phases into one period. a) Ideal case, whereby $P = 1$ b) Samples are distributed over $P = 10$ periods so that the amount of different angular phases by a factor of $g = gcd(18, 10) = 2$. c) Samples are distributed over $P = 11$ periods so that $g = gcd(18, 11) = 1$, which leads to the same angular phases as in a).

the theoretical maximal distance between two angular phases recorded with the integer frequency f_s. The mapped angular phases for each integer f_s are given in $A_{f_s}(n)$ and the difference towards the succeeding angular phase by:

$$D_{f_s}(n) = A_{f_s}(n+1) - A_{f_s}(n) \quad for \quad n = 1...N \tag{6.10}$$

In the next step the maximum difference is selected for all f_s

$$E(f_s) = max(D_{f_s}(n)) \tag{6.11}$$

The sampling frequency f_s is chosen, for which $E(f_s)$ is minimal. An additional constraint for the sampling frequency results from the faulty angular phases α_{err} (described in section 6.2). Therefor the sampling frequency should not exceed 4095 times the actuation

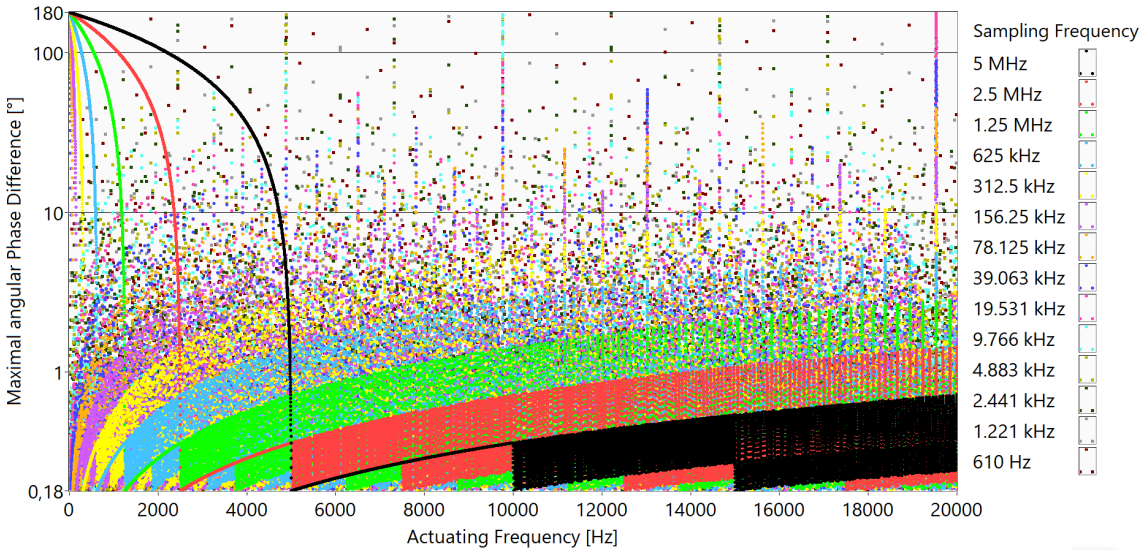

Figure 6.8: Maximal theoretical phase gap dependent on the actuating frequency $\mathbf{f_a}$ when measuring $\mathbf{N = 1000}$ samples at each pixel for every possible sampling frequency $\mathbf{f_s}$ according to Equation 6.12.

frequency ($f_s < 4096 \cdot f_a$) in order to avoid two successive erroneous angular phases, which would clearly increase the difficulty of the identification of those. The choice of sampling frequency in the here described experiments is further limited by the PSV to the main frequency of 10 MHz and the down-sampled frequencies

$$f_{ds} = \frac{10\,\text{MHz}}{2^n} \quad \text{for} \quad n = 0, 1, 2, 3, \ldots. \tag{6.12}$$

Figure 6.8 shows the maximal angular phase gap between measured samples for $N = 1000$ in dependence of the actuating and the sampling frequency. The graph clearly indicates that $f_s \leqslant N \cdot f_a$, because at least one period needs to be measured in order to reconstruct the periodic image sequence. For the lowest frequency of 1 Hz, it will be necessary to record more than 1 second at each pixel using a sampling frequency below 1000 Hz. In order to decrease measurement time, the highest possible sampling frequency with a reasonable error needs to be chosen for every actuated frequency. The graph also reveals a clear behavior of the phase error when the $N = 1000$ samples are distributed over 1-2 periods of the actuated sine, which leads to a maximal phase error of 0.36° (The curve of $f_{ds} = 5$ MHz (black) shows this behavior in the interval $f_a = [5\,\text{kHz}; 10\,\text{kHz}]$). This principle is used to select the largest suitable sampling frequency in the range $f_a = [1\,\text{Hz}; 10\,\text{kHz}]$. Above the phase error for all fast sampling frequencies, which lead to a measurement time below 50 ms, is calculated to chose the best.

6.3 Analysis Software

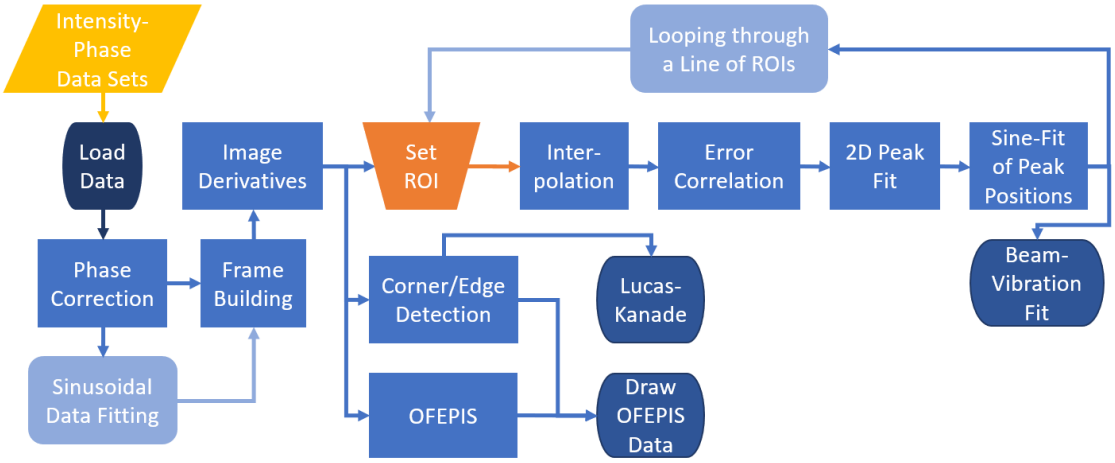

Figure 6.9: Program flow chart of the analysis software.

In order to extract the lateral vibrations out of the recorded data by the PSV an analysis software was built using the LabVIEW environment from National Instruments (NI). After loading the data file, the software needs to create a periodic image sequence by constructing frames from of the phase related intensity data. Hereby the erroneous phase data (see section 6.2) must be corrected in advance. Next, it determines temporal and spatial image derivatives (section 3.1) of all frames in the sequence, which contain the motion information, since they are a measure of change in the image sequence. Based on this it provides three different methods to reveal oscillating motion from this image sequence and its derivatives. The mainly developed and most advanced technique within the program is the TM, which shifts a region of interest (ROI) over all frames determining the best correspondence. Additionally the Lucas-Kanade algorithm was implemented as an rough estimate of motion and the OFEPIS-algorithm was implemented to provide a motion estimate for every pixel rather than only a ROI. Figure 6.9 shows the general program flow of the analysis software.

6.3.1 Frame Building

As discussed before the firmware of the PSV was upgraded so that it is able to provide a data set of N intensity-phase value pairs $[I_{x,y}(n); \varphi_{x,y}(n)]$ for each pixel of the scanned image. The aim is to construct 2D-frames, which correspond to equal distributed angular phases, whereby T gives the amount of frames and $\Delta\varphi = {}^{2\pi}/_{T}$ the phase shift between

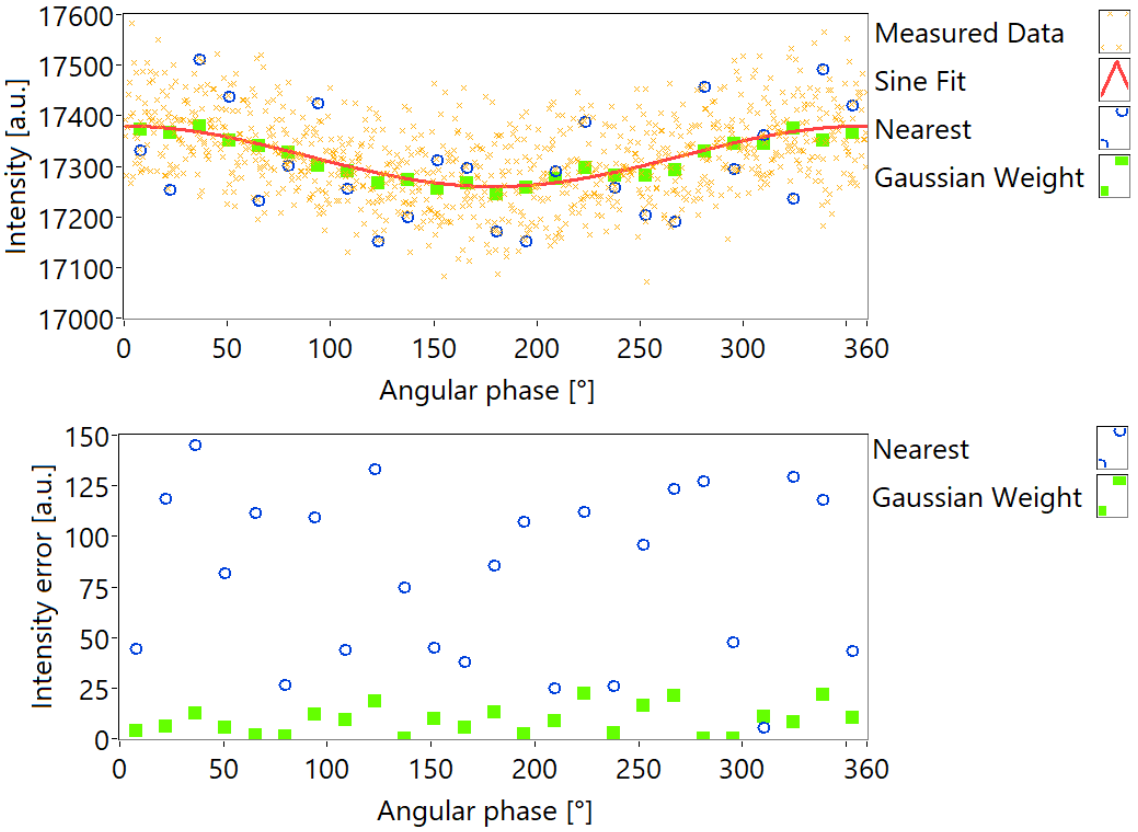

Figure 6.10: Measured raw data at one pixel from which intensity values for all $T = 25$ frames are constructed using different methods. Orange plots the intensity over the angular phase. Red shows a sinusoidal fit of the measured data. Blue indicates the intensity values of the nearest measured angular phases to the center phase. Green indicates the intensity values determined by Gaussian weighting.

two frames. The number of frames T is chosen by the user and defines equal intervals $[t \cdot \Delta t; (t+1) \cdot \Delta t]$ with their center angular phases $\varphi_t = (1/2 + t) \cdot \Delta t$ for $t = 0 \ldots T - 1$. Since the PSV does not offer the opportunity to directly trigger at T certain angular phases, N angular phases are measured (whereby $N \gg T$) to reconstruct the intensity values at the defined angular phases φ_t of interest.

Nearest Measured Angular Phase

The first method was choosing the intensity value of the nearest measured angular phase to the center φ_t for each of these T intervals. The deviation of the angular phase decreases with the increasing amount N of measured data points. Unfortunately for small intensity amplitudes the noise envelope (see Figure 6.10) corrupts the intensity values massively. Another drawback of this method is, that most of the recorded data remains

unused.

$$I(\varphi_t) = I(min(|\varphi_n - \varphi_t|)) \tag{6.13}$$

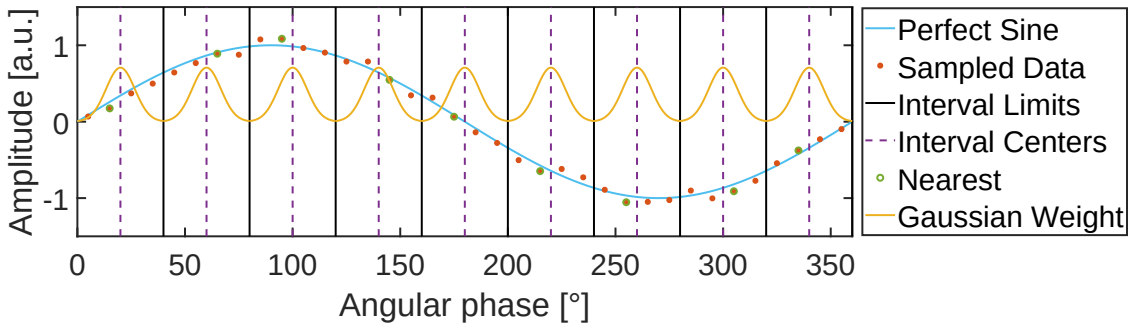

Figure 6.11: Theoretical reconstruction of the oscillation using nearest neighbors with random data. a) Blue: One period of the actuated sine. Red: $N = 36$ randomly measured angular phases. The intervals for each frame are presented. Purple: Centers φ_t of the $T = 9$ intervals. Green: Measured angular phases, which are each closest to at least one center. Yellow: Gaussian weights for each interval.

Weighted Averaging

The weighted averaging frame building uses all measured information to reduce noise. The weighting corrects for the fact that the measured samples have different angular phase shift towards the center angular phases φ_t. Only the values I_n corresponding to angular pases φ_n within the interval around the center angular phase φ_t are taken into account to estimate $I(\varphi_t)$. Figure 6.10 clearly indicates the reduction of noise compared to the nearest angular phase method.

$$I(\varphi_t) = \frac{\sum_n I(\varphi_n) \cdot w_n}{\sum_n w_n} \quad \text{for} \quad t \cdot \Delta\varphi < \varphi_n < (t+1) \cdot \Delta\varphi \tag{6.14}$$

Sinusoidal Weight The weighting function consists out of a sine to an even power, which is compressed by the factor $T/2$ in a way that one period fits exactly one interval. The FWHM can be adjusted by varying the exponent p in Equation 6.15, whereby p only accepts even integers.

$$w_n = sin^p\left(\frac{T}{2} \cdot \varphi_n\right) \quad \text{with} \quad p = 2, 4, 6, 8 \ldots \tag{6.15}$$

Gaussian Weight For each interval the mean of the Gaussian is set to the center angular phase $\mu = \varphi_t$. In Equation 6.16 The standard deviation (STD) σ scales the FWHM proportionally and can be freely chosen. Here $\sigma = {}^{\Delta t}/_{6}$ is used, so that the $\pm 3\sigma$ - range equals Δt [24].

$$w_n = \frac{1}{\sigma\sqrt{2\pi}} \cdot \exp\left(-\frac{1}{2}\left(\frac{\varphi_n - \varphi_t}{\sigma}\right)^2\right) \tag{6.16}$$

Sinusoidal Fit

A sinusoidal fit of the intensity plotted over the angular phase as in Figure 6.10 could also be used to reduce the noise and build any amount of frames. Hereby all data points (e.g. $N = 1000$) are equally considered, which is an advantage compared to the Gaussian weighting method. Additionally, a sinusoidal fit can be described by only three parameters: The amplitude, the phase and the offset, which would strongly decrease the amount of data to be stored or processed. However the a priori assumption that the intensity signal at one pixel follows the shape of a sine does not hold for larger amplitudes (compare with the KE-method), since it saturates in a high or low reflection value. The much longer computing time of the fitting algorithm suggest to rather use the Gaussian weighting method also for small vibration amplitudes, for which the intensity signal could be approximated as a sine.

Choice of Parameters

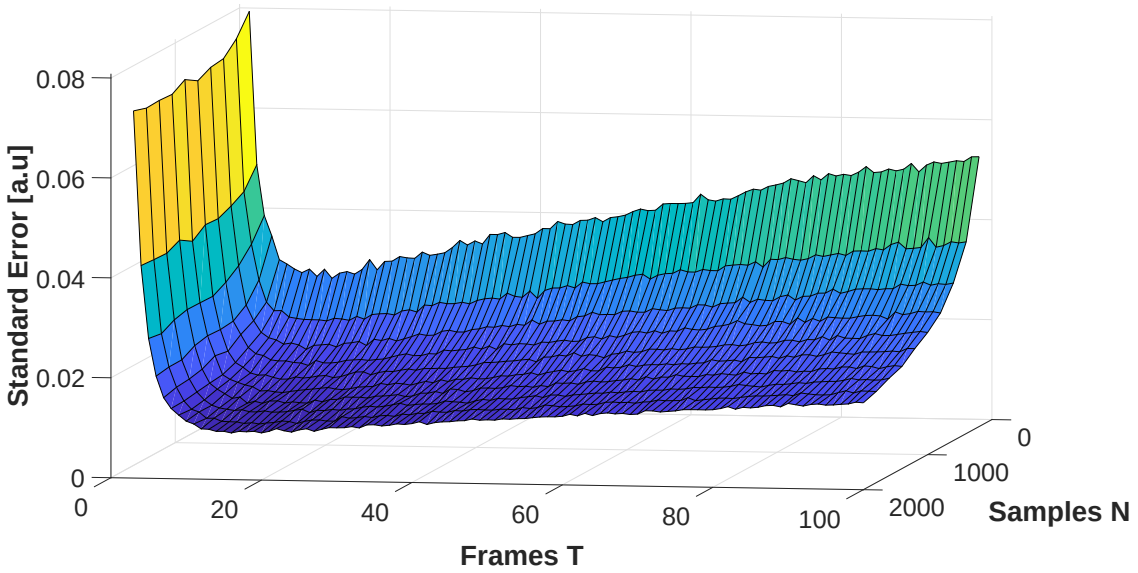

Figure 6.12: Standard error in dependence of the number of frames T and the number of recorded samples N at each pixel assuming sinusoidal intensity signals with normal distributed noise, which is estimated according to the measurement data seen in Figure 6.10.

Figure 6.12 shows a simulation of the standard error in dependence of the number of reconstructed frames T and the number of recorded intensity-phase pairs N at each pixel. Hereby the Gaussian weighting was used to reconstruct the intensity for a specific frame with 6σ equaling the interval size. A sinusoidal intensity signal was with normal distributed noise was constructed and sampled at N randomly distributed angular phases (actually this N measured angular phases follow a pattern according to subsection 6.2.1). In order to minimize the standard error, the number of frames T should be in the range of $10 < T < 30$. A higher number of recorded samples N leads always to a smaller standard error, but also to a longer measurement time and bigger data to be stored. Therefore, the number of samples recorded at each pixel was chosen to be $N = 1000$ as default.

6.3.2 Image Derivatives

The analysis software computes all of the following image derivatives in Figure 6.13 according to the theory in section 3.1.

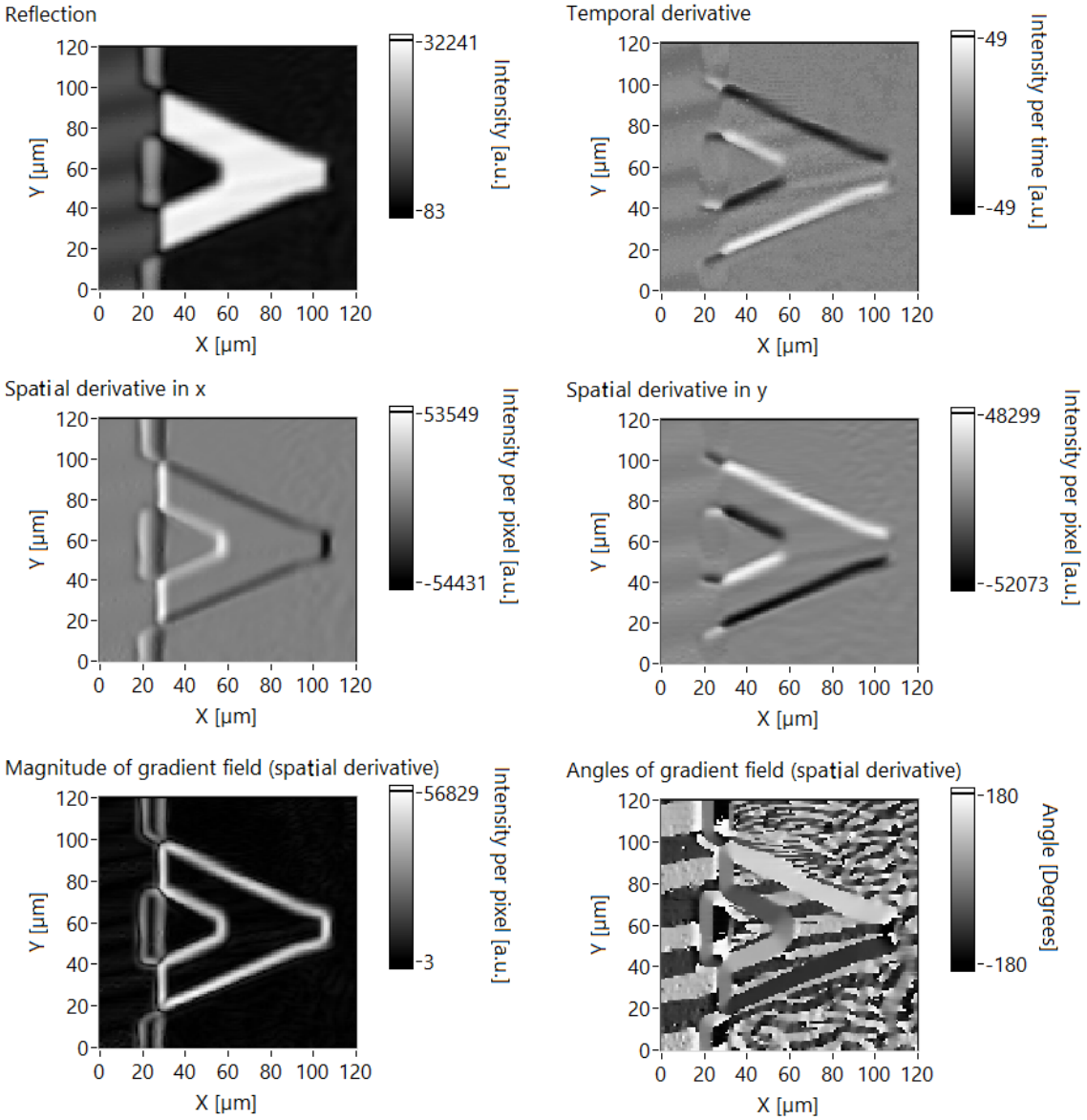

Figure 6.13: Image derivatives of a laterally oscillating, delta shaped cantilever a) Reflection image b) Temporal derivative of the reflection image sequence revealing motion in y-direction. c) Spatial derivative in x-direction d) Spatial derivative in y-direction e) Magnitude field of the gradient field (spatial derivative) f) Angle field of the gradient field (spatial derivative) All images are given with 1 µm resolution.

6.3.3 Template Matching

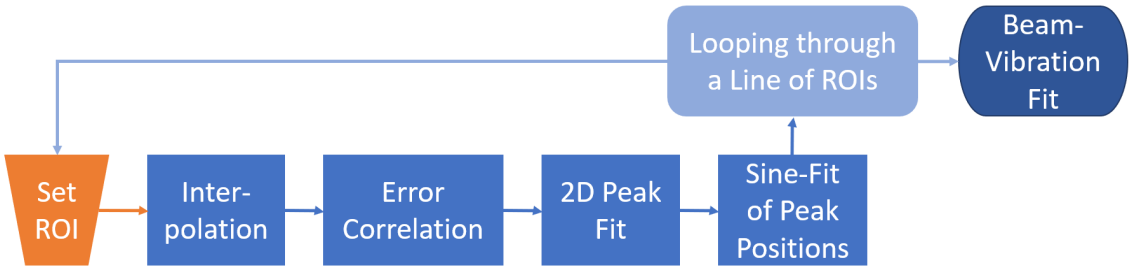

Figure 6.14: Workflow of TM-algorithm with single stages. Defining a ROI and a path on which it should be shifted allows repeating TM to get the vibration information along the path.

This technique is based on image correlation, whereby its aim is to find the displacement of the features within two successive frames. It asks the question: How does an image need to be shifted to show the same features at the same positions as in the template image. The shift-position with the best match corresponds to the displacement, which occurred in between the two frames. This method only works under the following assumptions:

- The intensity of features does not change over time or when the feature is moved.
- Every feature in the region of interest moves equally (same direction and speed).
- The image moves only in x- and y-direction. Although correlation could also be done for zooming and rotation both would add another dimension with a lot of complexity and a significant increase in computing time. However here rotational motion is not expected at all and vertical motion, which equals zooming, is small enough to be neglected.
- The observing instrument does not move. With this method the relative motion between the object and observer is determined. So, if the motion of the observer is know the absolute motion of the object could also be determined. Here however, the observing instrument is fixed in order to directly determine the objects motion.

In order to reach the optimal sub-pixel resolution with the TM-technique, the following procedure of algorithms is applied (see Figure 6.14):

1. The user chooses a ROI on the microscopy image. The analysis software extracts

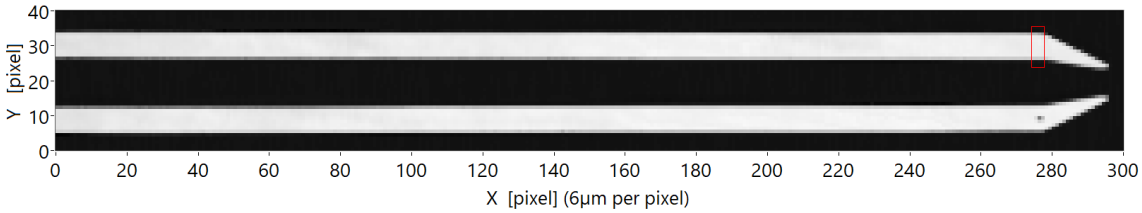

Figure 6.15: Microscopy image of microgripper arms with a selected ROI nearby the tip (right) of the upper arm. The ROI contains only horizontal edges, which only allows to determine the vertical vibrations accurately.

the ROI of one frame and additionally it extracts sub-images from all frames, which equal the ROI plus a frame of at least one pixel thickness.

2. The ROI and the framed sub-images are interpolated in order to get more sub-pixel information when comparing the images.

3. The ROI is shifted over all sub-images and the error correlation (EC) is calculated.

4. For each frame the shift position of the minimal error is extracted from the EC using a 2D-peak-fitting algorithm.

5. The determined optimal shift positions are plotted over the frame number and fitted with the expected sinusoidal oscillation in x- and y-direction. This provides the amplitude and direction of the vibration of the features seen in the ROI.

6. The program allows to define a path on a feature (e.g. a beam) so that it automatically does steps 1-5 for all defined ROI positions on this path, which can reveal vibrational modes of the feature.

Interpolation

The images can only be shifted by an increment of one pixel, because in between two pixels is no data. Interpolation provides data in between the pixels to enable shifting with sub-pixel increments, which is essential to observe sub-pixel movement. Therefore, interpolation increases the resolution, although no additional data is acquired. There are different interpolation methods:

- **nearest** An interpolated pixel gets the value from its nearest neighbor assigned.
- **bilinear** The value is determined using a linear fit based on the two linear fits of each pair of neighboring pixels

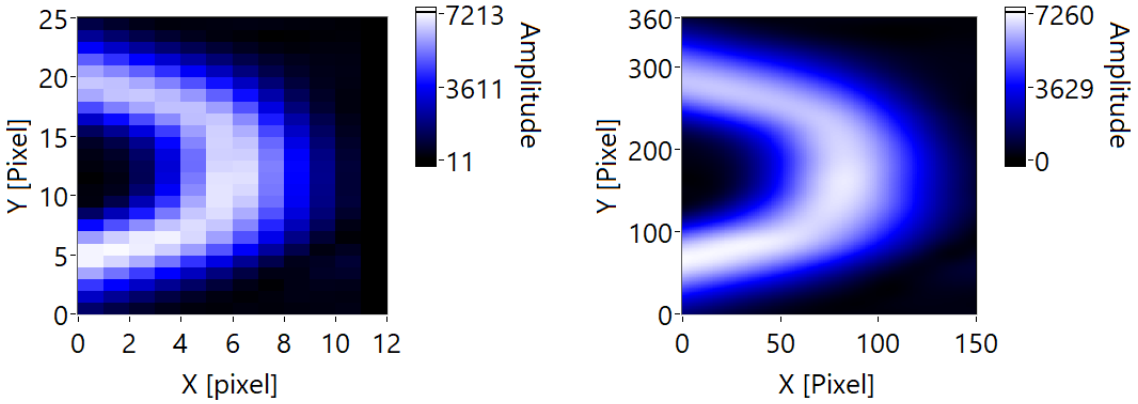

Figure 6.16: Interpolation of the ROI. Hereby the gradient of the actual measured reflection intensity images is used, since each edge in the reflection images appears as a line with two edges in the gradient images, thus providing a finer structure.

- **bicubic** The value is determined using a cubic fit based on the four cubic fits of each quadruple of neighboring pixels, whereby the first and second neighbors are taken into account, since a cubic fit needs at least four data points.

- **bicubic spline** The various bicubic polynomials for each pixel are connected with border constraints. At the border between two intervals the polynomial itself and its first and second derivative should each correspond to the polynomial of the next interval with its derivatives.

Error Correlation Method

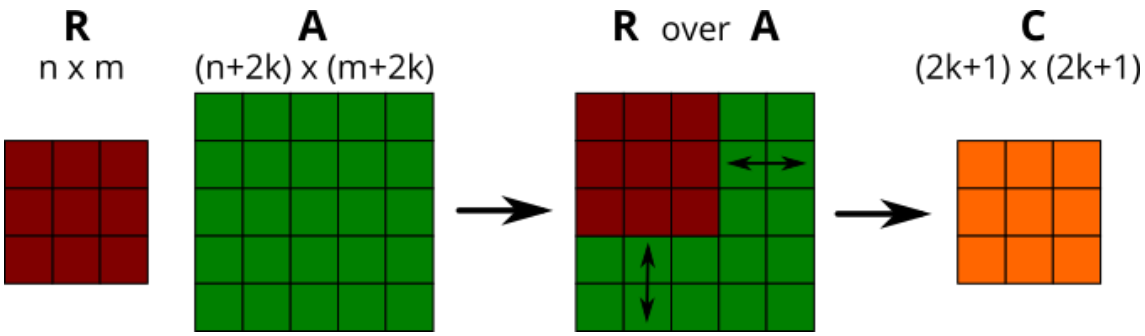

Figure 6.17: Image Correlation. The smaller region of interest R is shifted over the comparison region A. At each shift position the sub-images R and A_{sub} are correlated using the EC.

As seen in Figure 6.17 a region of interest R with $n \times m$ pixels of one frame is shifted over an comparison area A of $(n+2k) \times (m+2k)$ pixels of all frames in a way that for every shift-position all pixels of R are always over one pixel of A. The center position of R and

A are equal, but a frame of thickness k is added to construct A, whereby k is the maximal expected displacement in pixel. This rough estimate of the maximal displacement saves a lot of computing time as compared to using the whole image, because the correlation area can be reduced significantly. For every possible shift-position the region of interest R is correlated with the corresponding $n \times m$ sub-matrix A_{sub} of A and the correlation value is plotted over the shift-position. The error minimization is the main method to correlate R and A according to the equation:

$$C_{i,j} = \sqrt{\frac{\sum_{p=1}^{n} \sum_{q=1}^{m} \left(R_{p,q} - A_{p+i-1,q+j-1}\right)^2}{m \cdot n}} \tag{6.17}$$

In general, there are also other correlation methods such as e.g. the cross correlation. For this task the EC is chosen, since it weights the positive and negative deviations between R and A equally. Also this TM-procedure is done using the magnitude of the spatial gradient of the reflection intensity images, because this spatial derivative images converted edges into lines, which have two edges, so that more structural information can be compared in between the frames.

Determining Relative Displacement

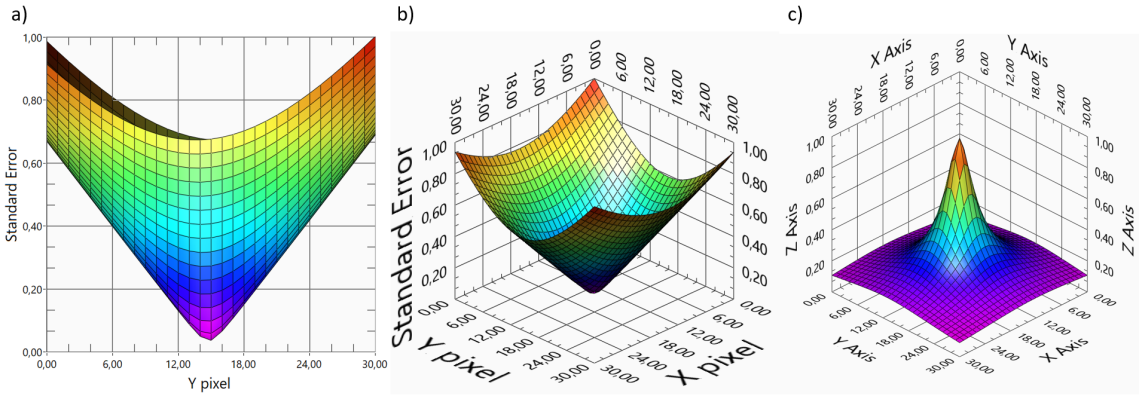

Figure 6.18: EC Images. The Error is given by the square root of the sum of squared differences, which is plotted over the shift position. All plots are normalized to a maximum height of 1. a) Side view indicating the linear increase of the error with increasing distance to the optimal match position. b) 3D perspective of EC image c) 3D perspective plot of reciprocal EC.

The correlation values for every shift position construct correlation images for every frame. These are a measure of how good the frames correlate with each shift position of

the reference frame. The position of the minimum in the correlation images corresponds to the relative displacement of the current frame compared to the reference frame. The displacement of each frame can later be used to reconstruct the harmonic oscillation. This peak in the correlation image could be determined using the integer pixel positions of the maxima, but this would limit the resolution to one interpolated pixel. In order to measure the displacement with even smaller resolution than an interpolated sub-pixel one needs to apply fitting methods to find the theoretical maximum, which lies in between the interpolated pixels. Figure 6.18 shows a correlation image and its 2D Gaussian fit calculated by the implemented 2D peak fitting algorithm described in section 3.2. The program offers four different peak fitting model functions:

$$
\begin{aligned}
f1(x,y,\mathbf{p}) &= \frac{H}{\sqrt{V+1}} \\
f2(x,y,\mathbf{p}) &= H\exp(-V) \\
f3(x,y,\mathbf{p}) &= H\sqrt{V} \\
f4(x,y,\mathbf{p}) &= H\cdot V \\
\text{with} \quad \mathbf{p} &= \left[H,\mu_x,\mu_y,\sigma_x,\sigma_y,\theta\right] \\
\text{and} \quad V &= a\left(x-\mu_x\right)^2 + 2b\left(x-\mu_x\right)\left(y-\mu_y\right) + c\left(y-\mu_y\right)^2 \\
\text{with} \quad a &= \frac{\cos(\theta)^2}{2{\sigma_x}^2} + \frac{\sin(\theta)^2}{2{\sigma_y}^2} \quad \text{and} \quad b = \frac{-\sin(2\theta)}{2{\sigma_x}^2} + \frac{\sin(2\theta)}{2{\sigma_y}^2} \\
\text{and} \quad c &= \frac{\sin(\theta)^2}{2{\sigma_x}^2} + \frac{\cos(\theta)^2}{2{\sigma_y}^2}
\end{aligned}
\tag{6.18}
$$

Harmonic Model Fitting

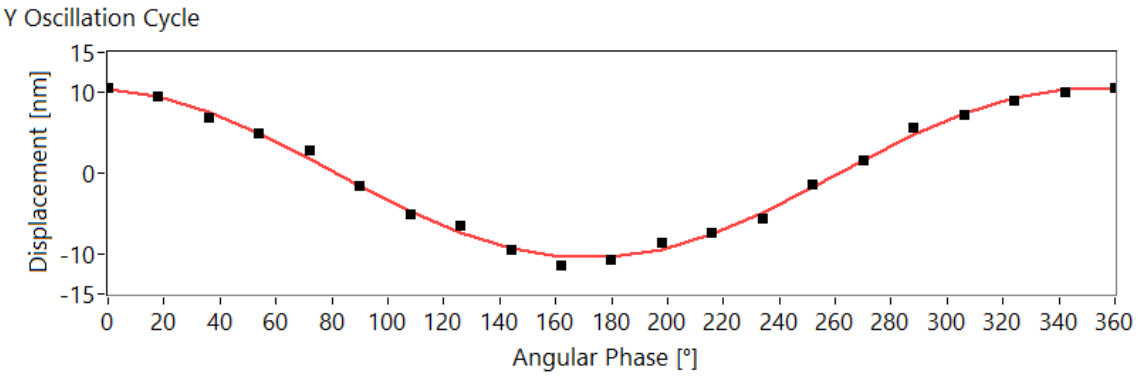

Figure 6.19: The mean positions of the 2D weighted peak fit give the optimal shift positions, which are plotted in this graph and fitted using a harmonic model, which is expected since the actuation is also harmonically.

The x- and y-means (μ_x, μ_y) of the 2D peak fit provide relative sub-pixel positions of the EC-minima for each of the T frames. An example of the x-means is plotted in Figure 6.19. A sine is fitted to the frame positions, since an harmonic oscillation is expected as outcome of a harmonic actuation. The amplitude and phase of these sinusoidal oscillations for the x-and y-direction describe the vibration of the features in the ROI giving the amplitude direction and relative phase to the actuation.

Line of ROIs

The program also offers to set a path on which the ROI is automatically shifted to defined positions. For each ROI the former steps are performed to get the amplitude and phase of the x- and y-vibration. These result can be plotted over the position of the ROI on the defined path. This method allows investigation of beams are similar structures as seen in

6.3.4 Lucas-Kanade Algorithm with Corner-/Edge Detection

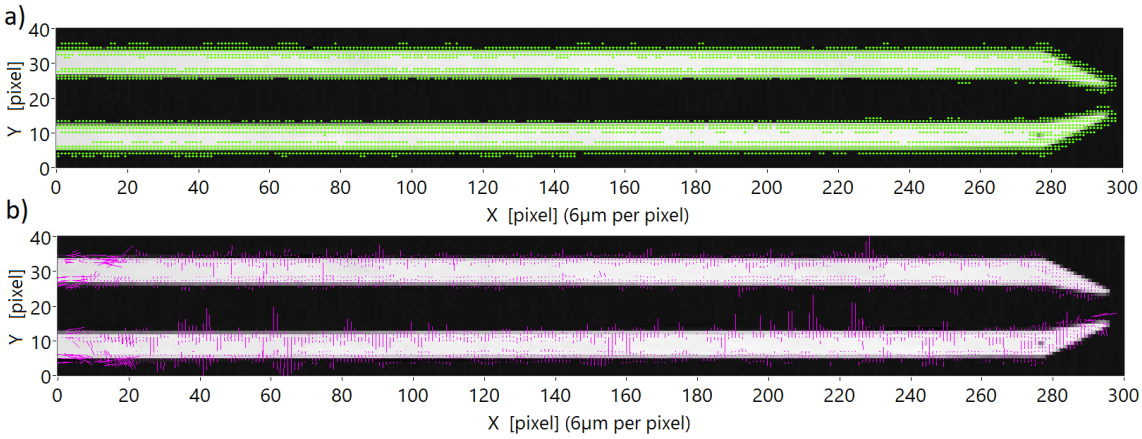

Figure 6.20: Example results of the edge detection algorithm and the Lucas-Kanade algorithm applied to an periodic image sequence of the two FT-G60 arms at $\mathbf{f_a} = 41\,212$ Hz, where the two arms oscillate at their second lateral bending mode. a) Edge detection algorithm to localize the interesting regions of the image sequence, since the optical flow algorithms obtain the most information from the edges and corners of image features. b) Motion estimate from one frame to its successive frame determined by the Lucas-Kanade algorithm, which is not able to reveal the second bending mode of the two microgripper arms, due to noise. Therefor the Lucas-Kanade algorithm could at most give a rough estimate and is not used furthermore.

A corner/edge detection algorithm combined with the Lucas-Kanade algorithm are also implemented according to section 4.1 and example results are shown in Figure 6.20. The edge detection gives a reasonable but rough result. The Lucas-Kanade algorithm does not

reveal the second bending mode, so that it is concluded that it can only provide a rough estimate if the sample meets certain quality criteria. It is not used further to investigate in-plane vibrations.

6.3.5 Implementation and Examples of the OFEPIS-Algorithm

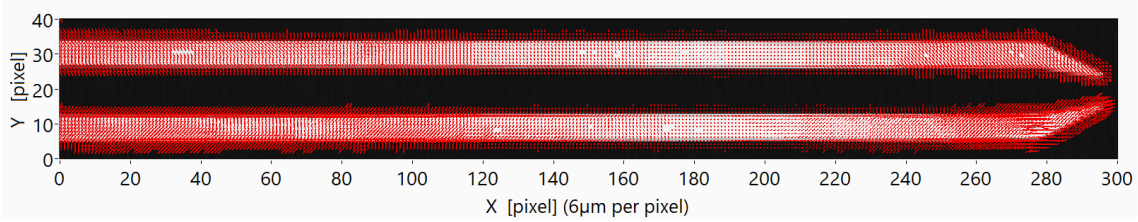

Figure 6.21: Motion estimate of the OFEPIS-algorithm revealing the second bending mode. The red lines indicate the direction and magnitude of the vibration at their respective pixel position. Hereby their lengths are exaggerated for visualization.

The OFEPIS algorithm is implemented according to section 4.2 and the iterative scheme, which is suggested by Li and Yang [14]. It provides motion estimation for every pixel of the image. In the analysis software the edge detection algorithm is used to display only the oscillation results of the interesting pixels. An example result is shown in Figure 6.21.

Chapter 7

Measurement Data and Evaluation

In order to evaluate and optimize the function of the algorithms in the written analysis program, an experimental setup was built using two PSVs, one to determine the lateral vibrations and the other was operated in out-of-plane mode as reference device (further described in chapter 5). Two different samples (described in section 5.3) were investigated using the developed experimental procedure (see chapter 6) in order to reveal lateral vibrations.

7.1 Bruker MLCT-O10 Cantilever F

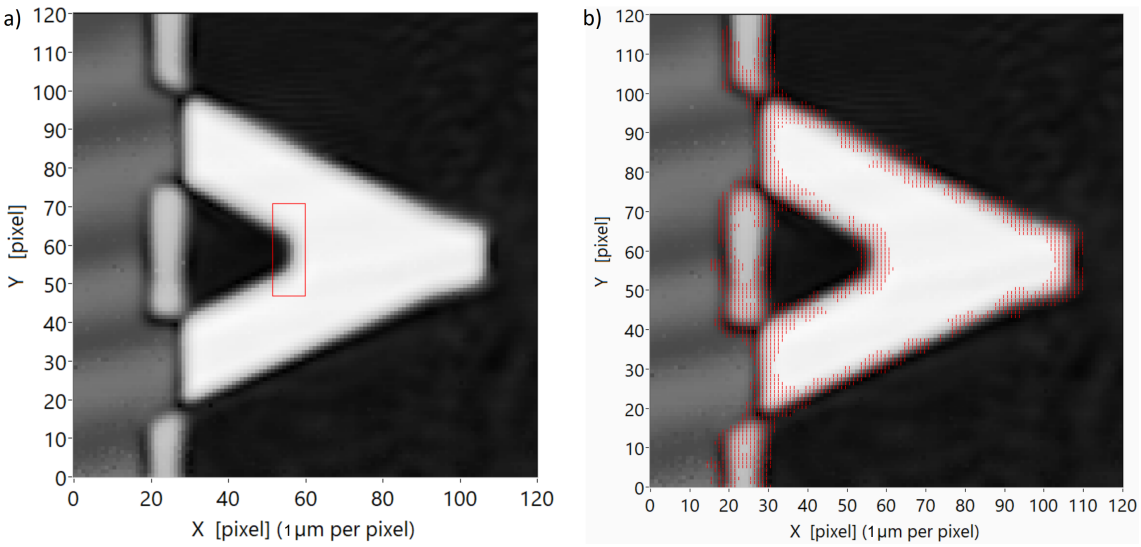

Figure 7.1: Measurement of a 10.08 nm vibration in y-direction of the Bruker MLCT-O10 cantilever F. a) Microscopy image, which was also used to define a ROI in order to use the TM-technique to reveal the lateral y-vibration. b) Qualitative results of the OFEPIS-algorithm which clearly reveal the vibration in y-direction.

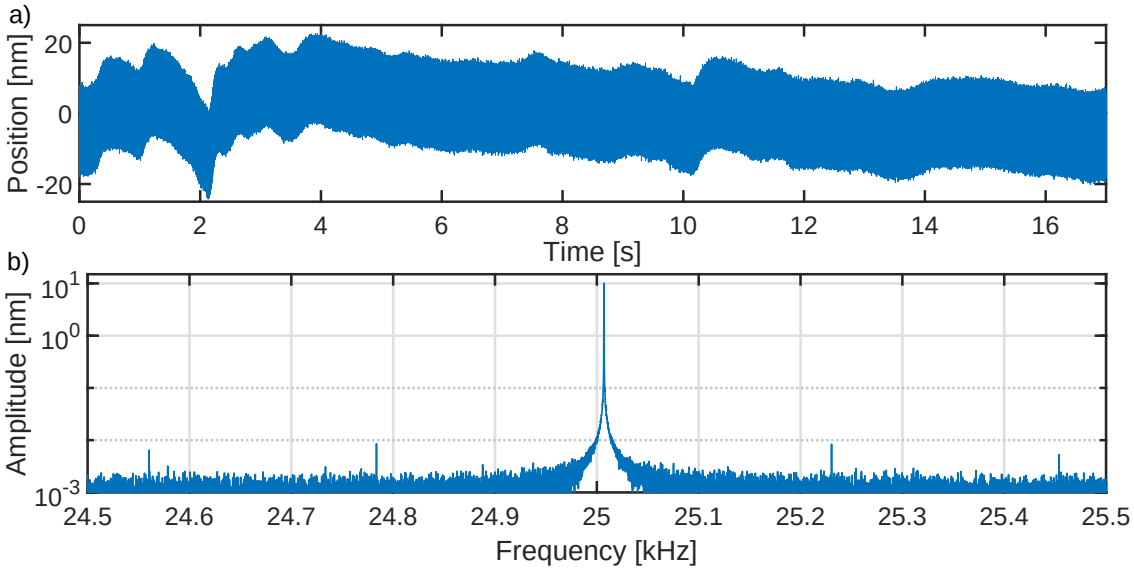

Figure 7.2: Reference measurement using a PSV from aside which revealed a 10.08nm vibration amplitude in y-direction of the Bruker MLCT-O10 cantilever chip excited at $\mathbf{f_a = 25007}$ Hz. a) Recorded position with the sampling frequency $f_s = 156.25$ kHz. The envelope of the position signal also fluctuates due to low frequency mechanical noise (motion of desk etc.). b) FFT from the position signal revealing the averaged semi-amplitude at the actuated frequency.

The delta shaped cantilever F of the Bruker MLCT-O10 cantilever chip was actuated in y-direction at a frequency $f_a = 25\,007$ Hz with a 10.08 nm vibration amplitude of the actuator stage (described in section 5.2). As can be seen in Figure 7.2 this was determined measuring the position signal using a second PSV from aside and calculating the FFT of it. Figure 7.1 a) displays the microscopy image of the cantilever F and a ROI, which was further investigated using the TM-method. Figure 7.1 b) shows the qualitative results of the OFEPIS-algorithm on the measured image sequence of the cantilever F, which clearly indicates that the complete cantilever oscillates together with the actuator stage in y-direction. Calculating the in-plane vibration of the cantilever at the given ROI using the TM-method of the analysis software described in section 6.3 leads to the following results shown in Figure 7.3. The two graphs indicate a clearly measurable oscillation in y-direction of ≈ 10.5 nm amplitude and no oscillation in x-direction, since the signal of the optimal shift positions of each frame is noisy with a total fluctuation of ≈ 1.4 nm. In order to test the accuracy and stability of the implemented TM-method 42 different ROIs at 9 different positions on the cantilever were investigated and the results are shown in the Table 7.2.

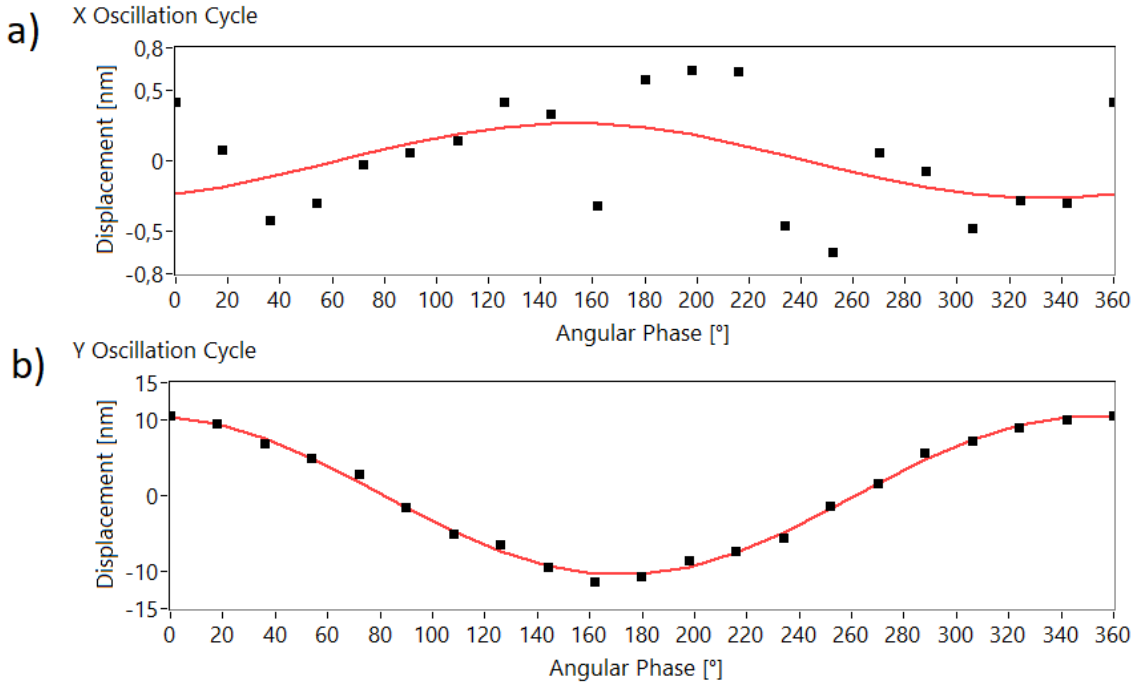

Figure 7.3: Optimal matching positions from TM which are fitted sinusoidally. a) Since there was no movement in x-direction, the measured movements are due to noise, which is below 1 nm. b) In y-direction the sinusoidal fit suits very well and reveals a oscillation of the sample with a semi-amplitude of ≈ 10.5 nm.

ROI - POSITION		Y-Amplitude	X-Amplitude	Total Amplitude	Direction α
TOP	μ	11.21 nm	0.43 nm	11.22 nm	2.2°
	σ	0.21 nm	0.11 nm	0.21 nm	0.5°
$N = 9$	σ [%]	1.8 %	25 %	1.8 %	0.15 %
CENTER	μ	10.40 nm	0.22 nm	10.41 nm	1.2°
	σ	0.13 nm	0.12 nm	0.13 nm	0.7°
$N = 15$	σ [%]	1.2 %	55 %	1.2 %	0.19 %
FOOT	μ	10.36 nm	0.31 nm	10.36 nm	1.7°
	σ	0.12 nm	0.11 nm	0.12 nm	0.6°
$N = 9$	σ [%]	1.2 %	35 %	1.2 %	0.16 %
ALL	μ	10.62 nm	0.33 nm	10.63 nm	1.8°
	σ	0.42 nm	0.16 nm	0.42 nm	0.8°
$N = 42$	σ [%]	4.0 %	47 %	4.0 %	0.22 %

Table 7.1: The TM-method is used on 42 different ROIs which were recorded on 9 different positions. The three main positions are the top, the center and the left foot of the cantilever. The mean and the STD and the amount of samples N they are based on are stated. The STD is additionally calculated in percentage of the mean. For the direction the percentage is related to 360° and $\alpha = 0°$ is set to be in y-direction. All results of the TM-method are slightly higher than the measured reference amplitude, which could be due to non-perfect alignment of the interferometer head of the reference device. Also, the top of the cantilever was measured to oscillate more than the center and foot of the cantilever, which could be possible, since the top is the thinnest and most outer part of the cantilever.

7.2 Femtotools FT-G60 Microgripper

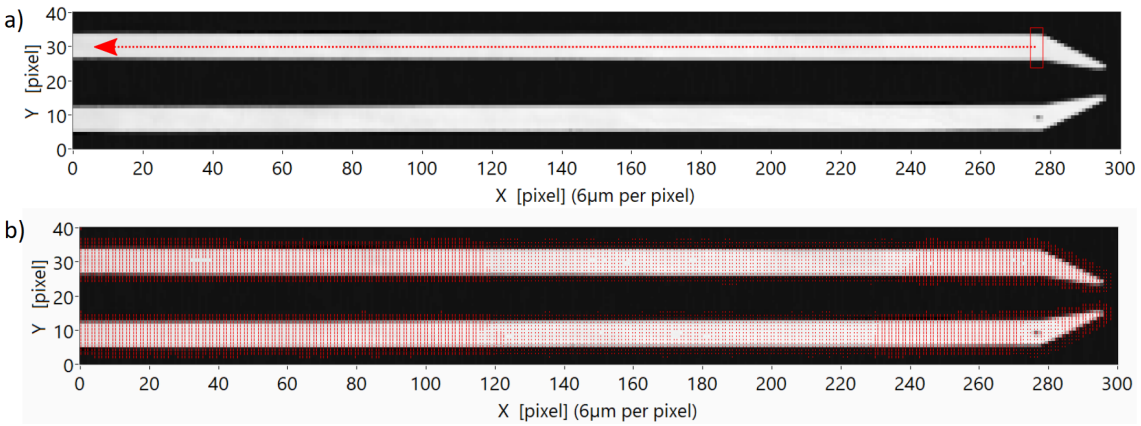

Figure 7.4: Optical flow estimate determined with OFEPIS-algorithm. The plot reveals the second lateral bending mode of the microgripper arms at 41 212 Hz, whereby the red vibration paths are amplified with the factor of 200. The increment of the x-,y-axis are pixels, whereby one pixel corresponds to 6 µm. The recorded image sequence does not show the complete microgripper arms, but only the part, which is outside the driving comb mechanisms.

The second evaluation measurement of the analysis software was performed by actuating the FT-G60 at $f_a = 41\,212$ Hz, where the dynamic response, which was determined with the KE-method, suggested a resonance frequency. The result from the OFEPIS-algorithm is presented qualitatively in Figure 7.4 b). It reveals the second bending modes of the two microgripper arms, with a vibrational node at around pixel 180 (corresponding to 1080 µm from the zero position). Figure 7.4 also indicates the starting ROI and the path on which it is shifted to determine the vibration of the whole left microgripper arm (in the figure it is the upper) using the TM-method. The results determined by the developed analysis program also clearly indicate the second bending mode of the microgripper arm. Figure 7.5 shows the in-plane measurement IP_m and the out-of-plane reference measurement OP_m, whereby additionally the Euler-Bernoulli beam model is fitted to each acquired data. The fit averages out the random noise of the accurate out-of-plane measurement of the PSV so OP_{Fit} is used as most reliable vibration behavior to compare all determination methods. Since the microgripper arm is not a homogeneous beam, but rather varies in thickness, the Euler-Bernoulli beam model is a rough approximation with gives still gives reasonable results.

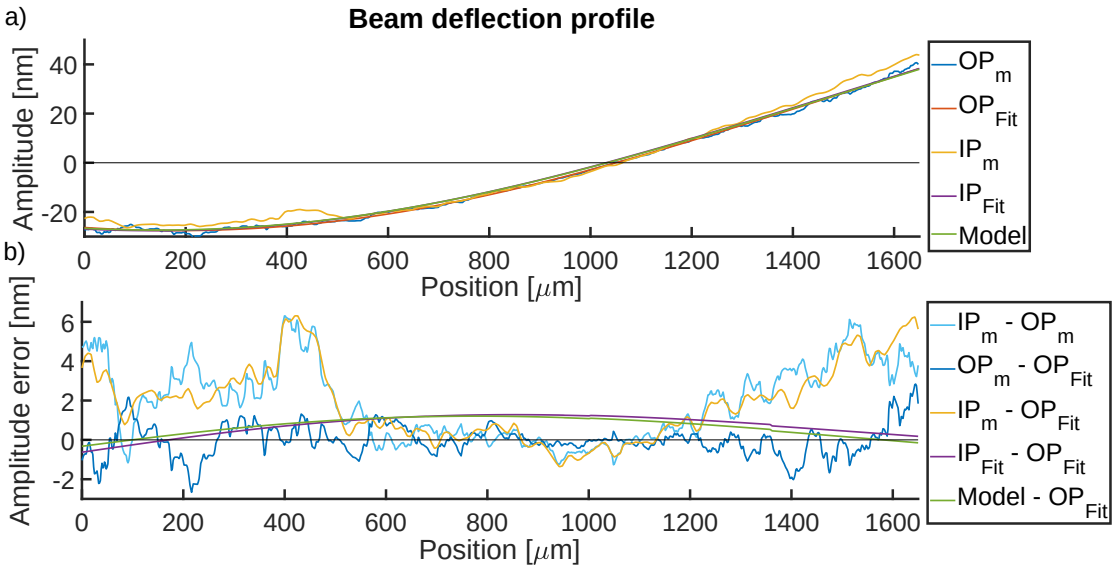

Figure 7.5: Deflection of 2nd bending mode of the left microgripper arm measured with different methods. Frequency: 41 212 Hz. The clamped end of the cantilever is approximately located at position −1200 µm, thus it is not seen. a) The in-plane measured deflection IP_m determined with the analysis software was fitted with the Euler-Bernoulli model shown as IP_{Fit}. As reference the deflection OP_m was measured with the out-of-plane scanning mode from the PSV from aside and also fitted shown as OP_{Fit}. The measured total length $L \approx 2847$ µm of the left microgripper arm determined from the microscopy image was used to calculate the theory model of the deflection assuming an amplitude of 38 nm. (Phase set to zero.) b) The amplitude error of all methods are given by the difference to the fit of the out-of-plane measurement OP_{Fit}, which filters out the noise from the accurate reference measurement. Additionally, the difference of the two measured deflections is plotted.

The excursion at every position of the beam oscillating at its second bending mode does only depend on its length and the actuated amplitude. Therefore, the length of the beam was measured and used to plot the theoretical model with an amplitude estimated by the other measurements. These three methods to determine the vibration behavior all depend on the length of the beam L, which is also one of the fitting parameters. Table 7.2 compares the length and vibration amplitude determined by the three approaches.

Method	Length L	Semi-Amplitude M
$\mathbf{IP_{Fit}}$	2860 µm ± 33 µm	38.33 nm ± 0.55 nm
$\mathbf{OP_{Fit}}$	2770 µm ± 8 µm	38.28 nm ± 0.12 nm
Microscopy	2847 µm ± 6 µm	

Table 7.2: Determined Length L and vibration amplitude M of the beam using three different methods. The error estimates of the fits are given by the 95% confidence intervals and the error of the length determined by the microscopy image is given by the pixel resolution of 6 µm.

Chapter 8

Discussion & Conclusion

8.1 Bruker MLCT-O10 Cantilever F

The measurement of the cantilever F from Bruker leads to resulting vibration amplitude of $\approx 10\,\text{nm}$ with an absolute accuracy of about $1.4\,\text{nm}$, which is about 14% of the vibration amplitude, whereby the optical resolution is $5\,\mu\text{m}$ and the scanning resolution is $1\,\mu\text{m}$. The deviation is not of random nature since it is systematically higher than the reference measurement. The inconsistency of the amplitudes measured at different positions of the same image sequence could be real differences, whereby the reference measurement was not sufficient, since it only measured the amplitude of the supporting actuator stage, which would allow different parts of the cantilever to oscillate differently.

8.2 Femtotools FT-G60 Microgripper

The PSV was able to clearly measure the 2nd bending mode of the microgripper arm. The peak amplitude of $\approx 38\,\text{nm}$ was determined with an error of below $1\,\text{nm}$ as it was compared to the reference measurement. The peak amplitude was about 150 times smaller than the pixel and optical resolution and the error is at about a thousandth of the pixel and optical resolution. The maximal deviation between the in-plane and the reference measurement are only slightly above $6\,\text{nm}$. The determined length of the microgripper arm with the different methods deviates only by about 4% around $\approx 2.8\,\text{mm}$. These results could be reached with an optical resolution of $5\,\mu\text{m}$ and a scanning resolution of $6\,\mu\text{m}$.

8.3 Error Sources of Template Matching

Uncertainties originate from various sources:

- Mainly uncertainties rise from the fact that amplitudes are extracted, which are about 100 times smaller than the optical and the scanning resolution.
- Vibrations induced by walking people in the room caused noise while the measurement setup recorded its data.
- The pixel-by-pixel recording of the data allows spatial drifts of the sample to cause huge deviations between different parts of the recorded images.
- The reference measurements are also noisy.
- The quality of the samples (in more detail below).

The quality of the samples strongly affects the accuracy of the TM-technique. Good quality is identified by the following characteristics:

- The microscopy image should show features of different reflection intensities, since the TM-technique uses the variation of intensity to determine in-plane vibrations.
- If more features vibrate equally the ROI can be set around all those. Hereby more information can be used to determine the in-plane vibration.
- The features of the sample need to be larger than the optical resolution of 5 µm of the PSV, because all structures below this threshold only appear blurry.
- The features should have a good contrast given by sharp edges and high reflection intensity differences.
- The in-plane vibration information is mainly extracted from the edges of features. Multiple edges orientated in different directions minimize the orientation error.

8.4 Conclusion

Altogether this work shows a proof of principle that lateral vibrations can be measured and extracted with the PSV and the TM-method and OFEPIS-algorithm, which are implemented in the described analysis software. These techniques allow the PSV to measure

lateral vibrations down to 10 nm, which is about 100 times smaller than pixel resolution and 500 times smaller than optical resolution. The good signal-to-noise ratio of the measurement leads to the assumption that the real limit is still smaller than this. The post processing software can in general also be used for image sequences recorded with other devices. Altogether the aim could be achieved to extend the function of the PSV to 3D measurements, whereby the resolution of the in-plane vibrations does not fully reach the one of the out-of-plane vibrations but comes adequately close to be sufficient for samples in the micrometer range. Different approaches of optical flow analysis were tested and compared to choose the best promising to be implemented in the resulting analysis software.

8.5 Comparison of Methods & Outlook

The Lucas-Kanade algorithm was implemented in order to compare it with other methods. The very noise results indicate, that this algorithm is not suitable to unveil very small vibrations of the tested samples. The OFEPIS-algorithm provides vibration values for every pixel of the image sequence, which is a big advantage. The time didn't reach to optimize and calibrate this algorithm to an extent that quantitative measurements were possible. However, it is still a helpful tool to provide a qualitative overview of the dynamic behavior of a sample. The TM-technique shows the best accuracy for small regions of the sample under the assumption that the investigated region vibrations uniformly. The reached resolution of in-plane vibration measurements compares to the $\approx$ 25 nm resolution of measuring the displacement of scattering surfaces described by Hercher et al. [25]. Using a charge-coupled device (CCD) camera with a resolution of 450 nm and an algorithm based on the shift Fourier theorem enabled Teyssieux et al. [26] to get to a resolution of down to 100 pm, whereby the ratio between optical resolution and vibration amplitude is about 10 times larger than the ratio of the here presented TM-method. In order to increase performance of the presented techniques to measure in-plane vibrations more kinds of samples need to be tested to show the general stability of the method. The whole procedure involves many different parameters, which still can be optimized. One of areas where an increase of performance could perhaps be achieved is the OFEPIS-algorithm, which still needs to be quantified. Also it is possible to build on the KE-techniques and develop methods to quantify them. Another new approach to unveil

lateral vibrations is described by Wadhwa et al. [27] in their paper about phase-based motion magnification. This could magnify the motion in the recorded image sequence of the sample in a first step and in a second step TM-methods could be performed on the magnified image sequence to extract quantitative information with increased resolution. However, the first test of this technique did not look very promising, since the motion magnification distorted the image, due to its unequal magnification of different features. Due to this issues the TM-method could not be used properly.

Bibliography

[1] Bernard Cretin, Bruno Serio, and Pascal Vairac. In-plane optical measurement of vibrations of mems: gradient methods using interferometry and image processing. In *Microsystems Engineering: Metrology and Inspection III*, volume 5145, pages 161–169. International Society for Optics and Photonics, 2003.

[2] U. Rabe, K. Janser, and W. Arnold. Vibrations of free and surface-coupled atomic force microscope cantilevers: Theory and experiment. *Review of Scientific Instruments*, 67(9):3281–3293, 1996. doi: 10.1063/1.1147409. URL https://doi.org/10.1063/1.1147409.

[3] D. Sarid. *Scanning Force Microscopy: With Applications to Electric, Magnetic, and Atomic Forces*. Oxford Series in Optical & Ima. Oxford University Press, 1994. ISBN 9780195092042. URL https://books.google.de/books?id=iILmCwAAQBAJ.

[4] Institut für Physik Fakultät V Carl von Ossietzky Universität Oldenburg. Michelson interferometer. *Modul Grundpraktikum Physik Teil II*. URL https://uol.de/fileadmin/user_upload/physik/ag/physikpraktika/download/GPR/pdf/Michelson_Interferometer.pdf.

[5] J. Muñoz Maciel, F. Javier Casillas Rodríguez, M. Mora-González, F. Gerardo, P. Lecona, V. Manuel, and D. Ramírez. Digital processing techniques for fringe analysis. In A.A. Banishev, M Bhowmick, and Jue Wang, editors, *Optical Interferometry*, chapter 1, pages 1–23. IntechOpen, Rijeka, 02 2017. ISBN 978-953-51-2956-1. doi: 10.5772/66474. URL https://www.intechopen.com/books/optical-interferometry/digital-processing-techniques-for-fringe-analysis.

[6] C.K. Kirkendall and A. Dandridge. Overview of high performance fibre-optic sensing. *Journal of Physics D: Applied Physics*, 37(18):R197, 2004. URL http://stacks.iop.org/0022-3727/37/i=18/a=R01.

[7] T. Suzuki, O. Sasaki, S. Takayama, and T. Maruyama. Real-time displacement measurement using synchronous detection in a sinusoidal phase modulating interferometer. *Optical Engineering*, 32(5):1033–1038, 1993.

[8] O. Sasaki, Y. Ikeada, and T. Suzuki. Superluminescent diode interferometer using sinusoidal phase modulation for step-profile measurement. *Applied optics*, 37(22): 5126–5131, 1998.

[9] D. Kroon. Numerical optimization of kernel based image derivatives. *Short Paper University Twente*, 2009. URL `http://www.k-zone.nl/Kroon_DerivativePaper.pdf`.

[10] I. Sobel. An isotropic 3x3 image gradient operator, Feb 2014. URL `https://www.researchgate.net/publication/239398674_An_Isotropic_3_3_Image_Gradient_Operator`.

[11] H. Guo. A simple algorithm for fitting a gaussian function [dsp tips and tricks]. 28:134–137, 09 2011. URL `https://www.researchgate.net/publication/252062037_A_Simple_Algorithm_for_Fitting_a_Gaussian_Function_DSP_Tips_and_Tricks`.

[12] R. Rojas. Lucas-kanade in a nutshell, 2018. URL `http://www.inf.fu-berlin.de/inst/ag-ki/rojas_home/documents/tutorials/Lucas-Kanade2.pdf`.

[13] C. Harris and M. Stephens. A combined corner and edge detector. In *Alvey vision conference*, volume 15, pages 10–5244. Citeseer, 1988.

[14] L. Li and Y. Yang. Optical flow estimation for a periodic image sequence. *IEEE transactions on image processing : a publication of the IEEE Signal Processing Society*, 19:1–10, Jan 2010. ISSN 1057-7149. doi: 10.1109/TIP.2009.2032341. URL `https://www.ncbi.nlm.nih.gov/pmc/articles/PMC3773580/pdf/nihms476971.pdf`.

[15] H. Rutishauser. The jacobi method for real symmetric matrices. *Numerische Mathematik*, 9(1):1–10, 1966.

[16] Tim Dabbs and Monty Glass. Fiber-optic confocal microscope: Focon. *Applied optics*, 31(16):3030–3035, 1992.

[17] E. Murphy and C. Slattery. Ask the application engineer—33 all about direct digital synthesis. *Analog Dialogue*, 38(3):8–12, 2004. URL `https://www.eecs.yorku.ca/course_archive/2007-08/W/3215/labs%20documentation/dds.pdf`.

[18] Zurich Instruments. Principles of lock-in detection and the state of the art, 2016. URL http://www.zhinst.com/sites/default/files/li_primer/zi_whitepaper_principles_of_lock-in_detection.pdf.

[19] Physik Instrumente (PI). Pica shear scheraktoren. URL https://www.physikinstrumente.de/fileadmin/user_upload/physik_instrumente/files/datasheets/P-111-P-153-Datenblatt.pdf.

[20] Thorlabs Inc. Piezoelectric chip specifications. URL https://www.thorlabs.com/drawings/213fc52d125fe398-A7D2DD44-C75F-CE85-B45A3E4DF74E28F4/PA3JE-SpecSheet.pdf.

[21] Bruker AFM Probes. Model: Mlct-o10. URL https://www.brukerafmprobes.com/p-3719-mlct-o10.aspx.

[22] A. Frangi and W. Scientific. *Advances in Multiphysics Simulation and Experimental Testing of Mems*. Computational and experimental methods in structures. Imperial College Press, 2008. ISBN 9781860948633. URL https://books.google.de/books?id=OLFgDQAAQBAJ.

[23] Alain Bosseboeuf, Cedric Bréluzeau, Fabien Parrain, Philippe Coste, Jean-Paul Gilles, Souhil Megherbi, and Xavier Le Roux. In-plane vibration measurement of microdevices by the knife-edge technique in reflection mode. In *Seventh International Conference on Vibration Measurements by Laser Techniques: Advances and Applications*, volume 6345, page 63451D. International Society for Optics and Photonics, 2006.

[24] Wolfram Alpha. Gaussian function. URL http://mathworld.wolfram.com/GaussianFunction.html.

[25] Michael Hercher and Geert J Wijntjes. Interferometric measurement of in-plane motion. In *Optical testing and metrology III: Recent advances in industrial optical inspection*, volume 1332, pages 602–613. International Society for Optics and Photonics, 1991.

[26] D Teyssieux, S Euphrasie, and B Cretin. Mems in-plane motion/vibration measurement system based ccd camera. *Measurement*, 44(10):2205–2216, 2011.

[27] Neal Wadhwa, Michael Rubinstein, Frédo Durand, and William T Freeman. Phase-based video motion processing. *ACM Transactions on Graphics (TOG)*, 32(4):80, 2013.

[28] SmarAct GmbH. Picoscan vibrometer, 2018. URL http://www.smaract.com/picoline/picoscan.

[29] SmarAct GmbH. Picoscan vibrometer, 2018. URL http://www.smaract.com/wp-content/uploads/2018/05/picoscan.jpg.

Appendix A

Femtotools FT-G6o Microgripper

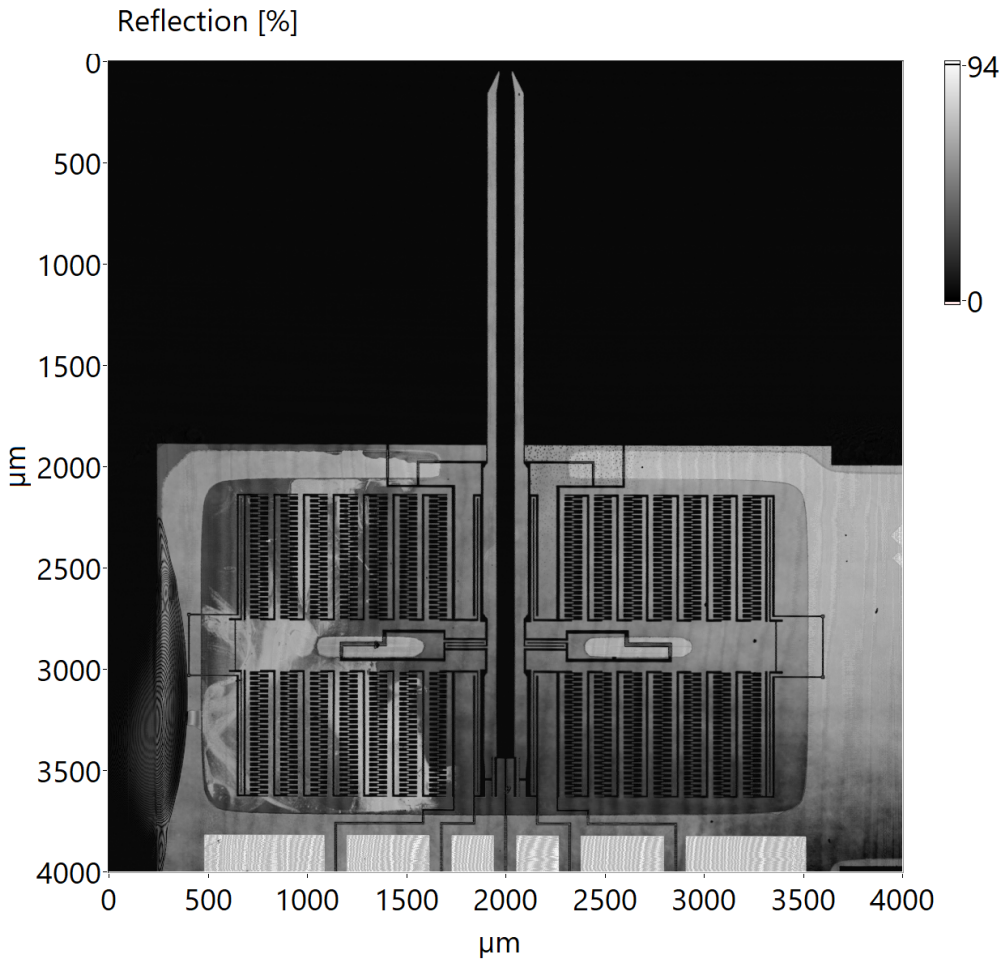

Figure A.1: Confocal microscopy image of FT-G6o Microgripper with one megapixel resolution. Scanning area: 4 mm x 4 mm.

FT-G60 Microgripper/ Nanogripper

Description

The Femtotools FT-G60 Micro-gripper is designed to handle micro- and nanoobjects. The initial opening of the gripper arms is 60um. The opening can be controlled with nano-meter precision. The maximum stroke is 60um (fully closed). Due to the electrostatic actuation principle there is no heating of the gripper arms.

Performance Characteristics (typical values)

Initial (maximum) gripper arm opening [um]:	60
Stroke [um]:	60
Maximum actuation voltage [V]:	150

Application Areas

- High precision pick-and-place operations
- Micro-assembly, Nano-assembly, micro-factories
- Micro-object sorting
- Sample preparation in biological and biomedical research
- Sample handling in a scanning electron microscope (SEM)
- Single cell handling

Electrical Interface

The FT-G gripper requires a high voltage power supply. A tunable voltage range up to 150V is recommended. Due to the electrostatic actuation principle virtually no current is flowing.
The gripper arms are electrically insulated from the rest of the device. The gripper arms can be set to GND or to any other potential using the Pin 3 (left arm) and Pin 4 (right arm).

Pinout

Pin1: Actuation voltage low (GND)
Pin2: Gripper left arm potential (GND)
Pin3: Actuation voltage HV (0-150V)
Pin4: Gripper rigth arm potential (GND)

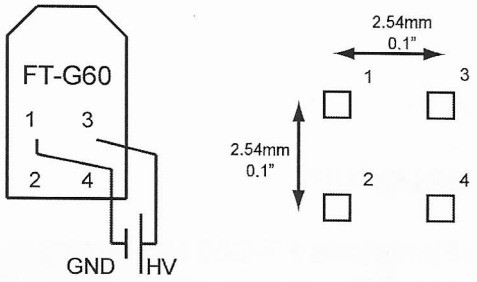

Dimensions

Dimensions in mm.

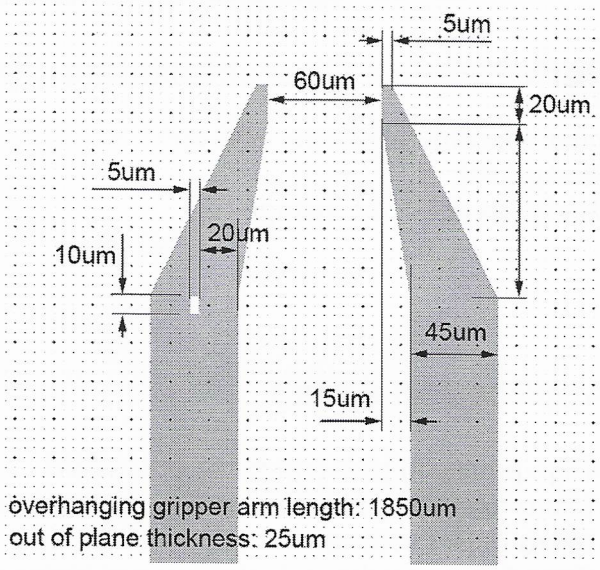

Appendix B

PICOSCAN Specifications

The content of the following datasheet is also found on SmarAct's webpage [28].

Figure B.1: SmarAct's PICOSCAN Vibrometer [29].

PICOSCAN

Megapixel Laser-Scanning Vibrometer

The **PICO**SCAN Vibrometer addresses the need for R&D and QC instrumentation that keeps pace with the ever increasing complexity of micromechanical systems. SmarAct's vibrometer is designed for megapixel imaging of vibrational modes of microscopic structures. This is achieved by raster-scanning a tightly focused laser beam of a Michelson interferometer over the sample to measure the vibrations for each pixel of the microscopic image. The **PICO**SCAN Vibrometer is equipped with a piezo-based sample shaker and a configurable digital lock-in amplifier to measure amplitude and phase of the vibrations from which bending modes of up to 2.5 MHz can be reconstructed.

The use of SmarAct's linear piezo positioners makes it possible to image structures with sizes from just a few µm up to 20 mm. A unique feature of the **PICO**SCAN Vibrometer is that the interferometer laser beam is used simultaneously to record a reflection image of the sample with a lateral resolution of 5 µm. This microscopic image is thus intrinsically aligned with the vibration measurements and a separate microscope imaging system is not required. The confocal measurement principle ensures that only light reflected from the focal plane will be detected while all out-of-focus light is suppressed. In combination with the infrared laser source this allows to image and to measure vibrations of a silicon structure even through a silicon enclosure.

KEY FEATURES

- Contactless measurement of vibrations of microscopic structures with pm resolution
- Imaging of vibrational modes of up to 2.5 MHz
- Megapixel imaging at 5 µm optical resolution, maximum field of view of 20 x 20 mm (larger ranges available on request)
- Integrated digital dual-phase lock-in amplifier
- Piezo based shaker stage for the actuation of vibrations plus the possibility to drive custom actuators
- Compact scanner (5.5 x 11.0 x 7.5 cm) that can be easily integrated into custom set-ups through a 25 mm diameter post mount (UHV compatible scanner on request)
- Delivered as a turnkey system including a granite base plate and software for data acquisition and analysis

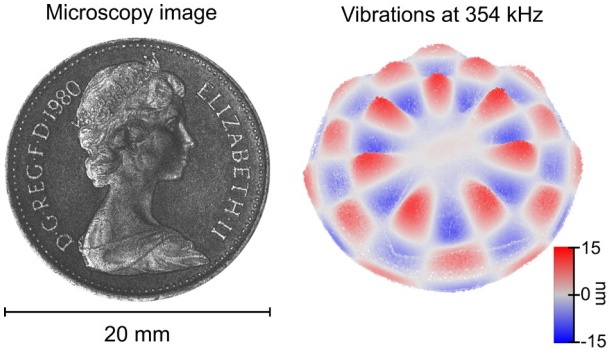

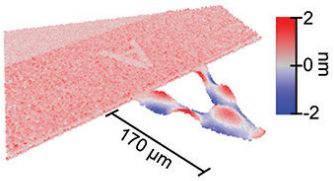

High bandwidth:
Complex higher order bending mode of a triangular AFM cantilever at 2.1 MHz

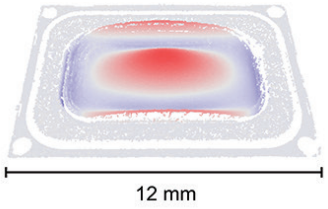

Large scan range:
Dynamics of a transparent membrane of a mobile phone loudspeaker at 12 kHz

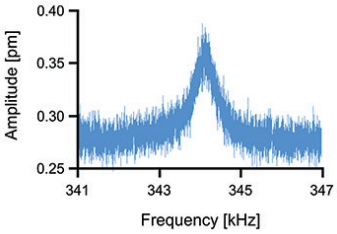

Picometer resolution:
Single point measurement showing sub-pm thermal fluctuations of a microcantilever

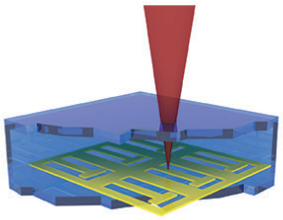

Measuring through silicon:
The confocal measurement principle makes it possible to measure vibrations through enclosures even if these are made from silicon

Vibration measurement	
Working principle:	Michelson interferometer, single mode fiber coupled
Measurement laser:	1550 nm DFB laser diode, stabilized (NIST traceable). Power output < 1 mW (laser class 1)
Laser spot diameter at focus:	7 µm
Resolution:	1 pm for single point measurements, 0.1 nm in imaging mode
Imaging mode:	Amplitude and phase images can be analyzed with the included software or exported
Single point mode:	FFT spectrum from 1 Hz - 2.5 MHz with max. 2.5 million points

Digital lock-in amplifier	
Frequency range:	500 Hz - 2.5 MHz
Reference signal:	Available through standard shaker stage and as output signal to drive custom actuators
Time constant:	Adjustable from 1 µs to 0.5 ms
Dynamic reserve:	> 100 dB

Optical microscope	
Working principle:	Confocal laser scanning using the interferometer's measurement laser
Focusing adjustment:	Manual or automatic with closed loop piezo drive
Lateral resolution:	5 µm
Min. pixel size:	1 µm
Max. image size:	20 x 20 mm
Max. number of pixels:	1000 x 1000
Typical acquisition time:	50 s for 128 x 128 pixels, 500 s for 1000 x 1000 pixels

Scanning motion system	
Working principle:	3 axes linear piezo drive, closed loop
Resolution:	1 nm
Repeatability:	30 nm
Max. travel:	20 mm (others on request)

Dimension and weight	
Controller:	2 units of each 33.0 x 27.0 x 7.0 cm (W x L x H), combined weight of 7.7 kg
Scanner mount:	Granite stone 15.0 x 20.0 x 4.0 cm (W x L x H) with stainless steel post 2.5 x 15.0 cm (Ø x H), 4.3 kg
Scanning stage:	5.5 x 11.0 x 7.5 cm (W x L x H), 0.3 kg
Shaker stage:	Stainless steel 8.0 x 1.5 cm (Ø x H), 0.5 kg

Appendix C

Fourier transform of knife edging intensity signal

The Fourier transform of the KE intensity signal $I(t)$ from Equation 6.5 is derived in the following. Since the interest lies only within the amplitudes of the positive frequencies, the phase offset is set to zero $\varphi_0 = 0$, all DC offset terms ($\bar{I}$, O_1 and O_2) are omitted directly and all negative frequency components $\delta(m\omega_a + \omega)$ are omitted in the end, resulting in the one sided Fourier transform $\mathfrak{F}^+\{I(t)\}(\omega)$.

$$\mathfrak{F}\{I(t)\}(\omega) = \int_{-\infty}^{\infty} I(t) e^{-i\omega t} dt \tag{C.1}$$

Substitution of $I(t)$ using Equation 6.5:

$$\mathfrak{F}\{I(t)\}(\omega) = \int_{-\infty}^{\infty} \left(\Delta I \cdot \operatorname{erf}\left(\frac{A_\perp \cdot \cos(\omega_a t) + d}{\sigma\sqrt{2}} \right) + \bar{I} \right) e^{-i\omega t} dt \quad \text{with} \quad \omega_a = 2\pi f_a \tag{C.2}$$

Taylor expansion of the error function:

$$\operatorname{erf}(x) = \frac{2}{\sqrt{\pi}} \sum_{k=0}^{\infty} \frac{(-1)^k x^{1+2k}}{(1+2k)k!} \tag{C.3}$$

Omitting the DC offset term $\bar{I}$ and inserting Equation 3 into Equation 2 with $x = \frac{A_\perp \cdot \cos(\omega_a t) + d}{\sigma\sqrt{2}}$:

$$\mathfrak{F}\{I(t)\}(\omega) = \int_{-\infty}^{\infty} \frac{2\Delta I}{\sqrt{\pi}} \sum_{k=0}^{\infty} \frac{(-1)^k \left(\frac{A_\perp \cdot \cos(\omega_a t) + d}{\sigma\sqrt{2}} \right)^{1+2k}}{(1+2k)k!} e^{-i\omega t} dt \tag{C.4}$$

Rearranging the order of the sum over k and the integral and moving all time constant terms out of the integral:

$$\mathfrak{F}\{I(t)\}(\omega) = \frac{2\Delta I}{\sqrt{\pi}} \sum_{k=0}^{\infty} \frac{(-1)^k}{(1+2k)k!} \left(\frac{A_\perp}{\sigma\sqrt{2}}\right)^{1+2k} \int_{-\infty}^{\infty} \left(\cos(\omega_a t) + \frac{\sigma\sqrt{2}}{A_\perp} d\right)^{1+2k} e^{-i\omega t} dt \tag{C.5}$$

The binomial formula states:

$$(a+b)^c = \sum_{l=0}^{c} \binom{c}{l} a^l b^{c-l} \tag{C.6}$$

Inserting Equation 6 into Equation 5 with $a = \cos(\omega_a t)$, $b = \frac{\sigma\sqrt{2}}{A_\perp} d$ and $c = 1 + 2k$:

$$\mathfrak{F}\{I(t)\}(\omega) = \frac{2\Delta I}{\sqrt{\pi}} \sum_{k=0}^{\infty} \frac{(-1)^k}{(1+2k)k!} \left(\frac{A_\perp}{\sigma\sqrt{2}}\right)^{1+2k} \int_{-\infty}^{\infty} \left(O_1 + \sum_{l=1}^{1+2k} \binom{1+2k}{l} \cos(\omega_a t)^l \left(\frac{\sigma d\sqrt{2}}{A_\perp}\right)^{1+2k-l}\right) e^{-i\omega t} dt \quad \text{with} \quad O_1 = \left(\frac{\sigma d\sqrt{2}}{A_\perp}\right)^{1+2k} \tag{C.7}$$

Omitting the DC offset term O_1, rearranging the order of the sum over l and the integral, moving all time constant terms out of the integral and moving all terms, which do not depend on l, out of the sum over l:

$$\mathfrak{F}\{I(t)\}(\omega) = \frac{2\Delta I}{\sqrt{\pi}} \sum_{k=0}^{\infty} \frac{(-1)^k}{(1+2k)k!} \sum_{l=1}^{1+2k} \binom{1+2k}{l} \left(\frac{A_\perp}{\sigma\sqrt{2}}\right)^l d^{1+2k-l} \int_{-\infty}^{\infty} \cos(\omega_a t)^l e^{-i\omega t} dt \tag{C.8}$$

Introducing mathematical boolean switch functions, which give 0 or 1 depending on the parity of their arguments:

$$s_e(x) = \frac{1+(-1)^x}{2} \quad \text{and} \quad s_o(x) = \frac{1+(-1)^{x+1}}{2} \quad \text{for} \quad x \in \mathbb{N} \tag{C.9}$$

Series representation of the cosine function raised to the power l. The boolean switch function is used to distinguish even and odd harmonic components within the sum over

m. The even components contain DC offset terms, which are given in O_2:

$$\cos(x)^a = \frac{1}{2^{a-1}} \left(O_2(a) + \sum_{m=1}^{a} s_e(a+m) \binom{a}{\frac{a-m}{2}} \cos(mx) \right) \quad \text{with} \quad O_2(a) = s_e(a) \binom{a-1}{\frac{a}{2}-1} \tag{C.10}$$

Inserting Equation 10 into Equation 8 with $a = l$ and $x = \omega_a t$ and omitting the DC offset term O_2:

$$\begin{aligned} \mathfrak{F}\{I(t)\}(\omega) = \frac{2\Delta I}{\sqrt{\pi}} \sum_{k=0}^{\infty} \frac{(-1)^k}{(1+2k)k!} \sum_{l=1}^{1+2k} \binom{1+2k}{l} \left(\frac{A_\perp}{\sigma\sqrt{2}} \right)^l d^{1+2k-l} \\ \int_{-\infty}^{\infty} \frac{1}{2^{l-1}} \sum_{m=1}^{l} s_e(l+m) \binom{l}{\frac{l-m}{2}} \cos(m\omega_a t)\, e^{-i\omega t} dt \end{aligned} \tag{C.11}$$

Rearranging the order of the sum over m and the integral, moving all time constant terms out of the integral and moving all terms, which do not depend on m, out of the sum over m:

$$\begin{aligned} \mathfrak{F}\{I(t)\}(\omega) = \frac{4\Delta I}{\sqrt{\pi}} \sum_{k=0}^{\infty} \frac{(-1)^k}{(1+2k)k!} \sum_{l=1}^{1+2k} \binom{1+2k}{l} \left(\frac{\sqrt{2}A_\perp}{4\sigma} \right)^l d^{1+2k-l} \\ \sum_{m=1}^{l} s_e(l+m) \binom{l}{\frac{l-m}{2}} \int_{-\infty}^{\infty} \cos(m\omega_a t)\, e^{-i\omega t} dt \end{aligned} \tag{C.12}$$

The Fourier transform of the cosine is given by:

$$\mathfrak{F}\{\cos(ax)\}(\omega) = \int_{-\infty}^{\infty} \cos(ax) e^{-i\omega t} dt = \pi(\delta(a-\omega) + \delta(a+\omega)) \tag{C.13}$$

Resolving the integral by inserting Equation 13 into Equation 12:

$$\begin{aligned} \mathfrak{F}\{I(t)\}(\omega) = 4\Delta I\sqrt{\pi} \sum_{k=0}^{\infty} \frac{(-1)^k}{(1+2k)k!} \sum_{l=1}^{1+2k} \binom{1+2k}{l} \left(\frac{\sqrt{2}A_\perp}{4\sigma} \right)^l d^{1+2k-l} \\ \sum_{m=1}^{l} s_e(l+m) \binom{l}{\frac{l-m}{2}} (\delta(m\omega_a - \omega) + \delta(m\omega_a + \omega)) \end{aligned} \tag{C.14}$$

Omitting the negative frequencies to result in the one sided Fourier transform of the KE-intensity signal and rearranging results in:

$$\mathfrak{F}^{+}\left\{I(t)\right\}(\omega) = \\ 4\Delta I\sqrt{\pi}\sum_{k=0}^{\infty}\frac{(-1)^{k}(2k)!}{k!}\sum_{l=1}^{1+2k}\frac{\left(\frac{\sqrt{2}A_{\perp}}{4\sigma}\right)^{l}d^{1+2k-l}}{(1+2k-l)!}\sum_{m=1}^{l}\frac{s_{e}(l+m)}{\left(\frac{l-m}{2}\right)!\left(\frac{l+m}{2}\right)!}\delta(m\omega_{a}-\omega) \tag{C.15}$$

Appendix D

Analysis Software GUI

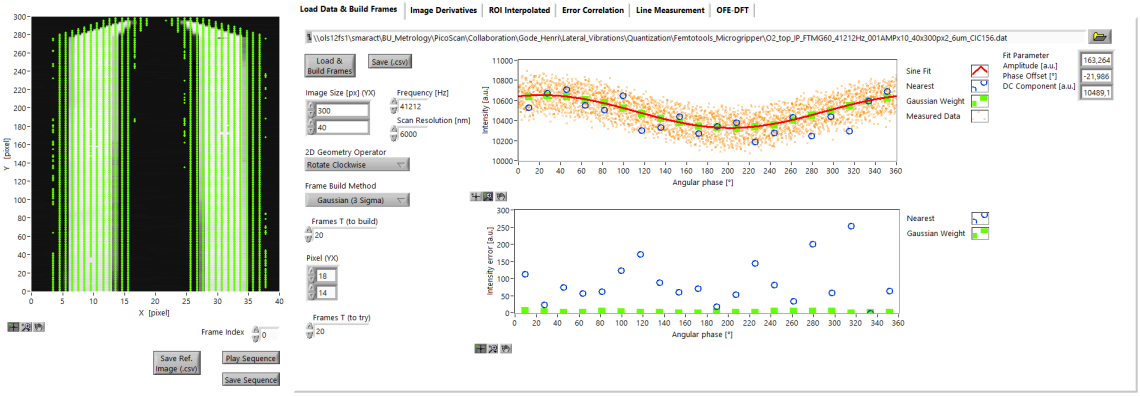

Figure D.1: Load data and build frames of image sequence.

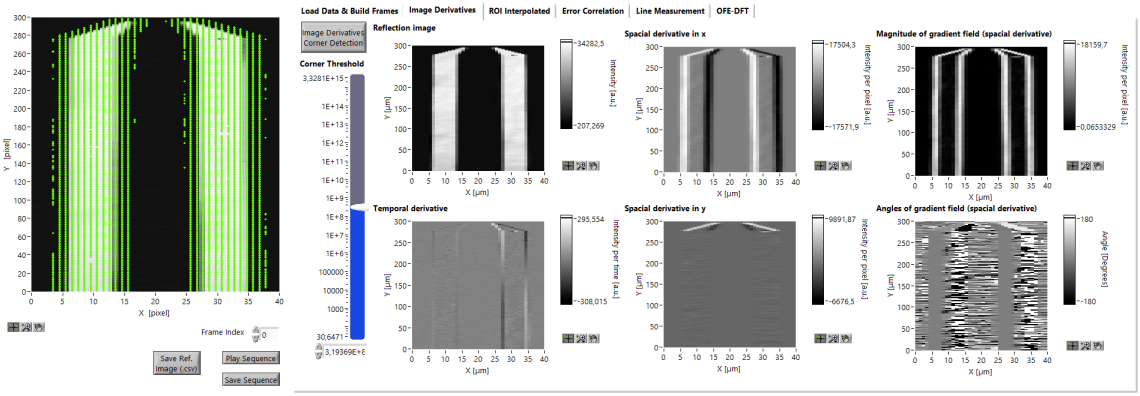

Figure D.2: Image derivatives and corner detection

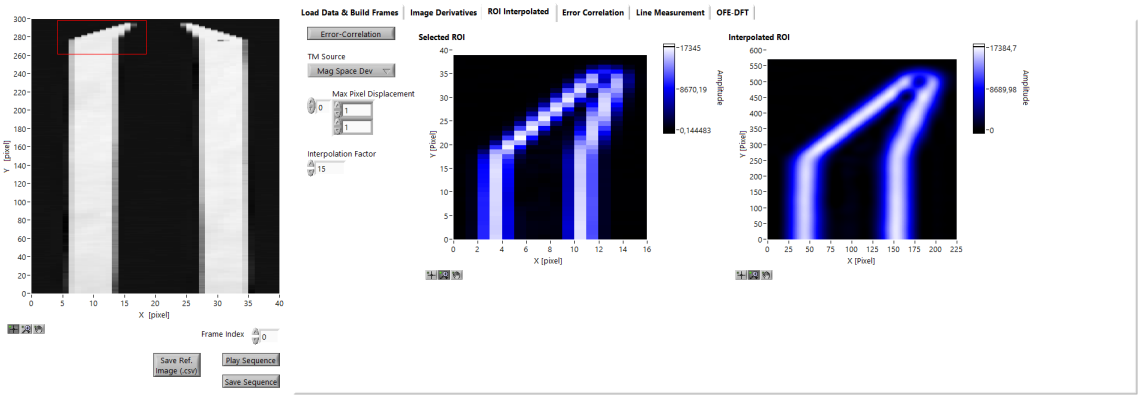

Figure D.3: Selecting ROI

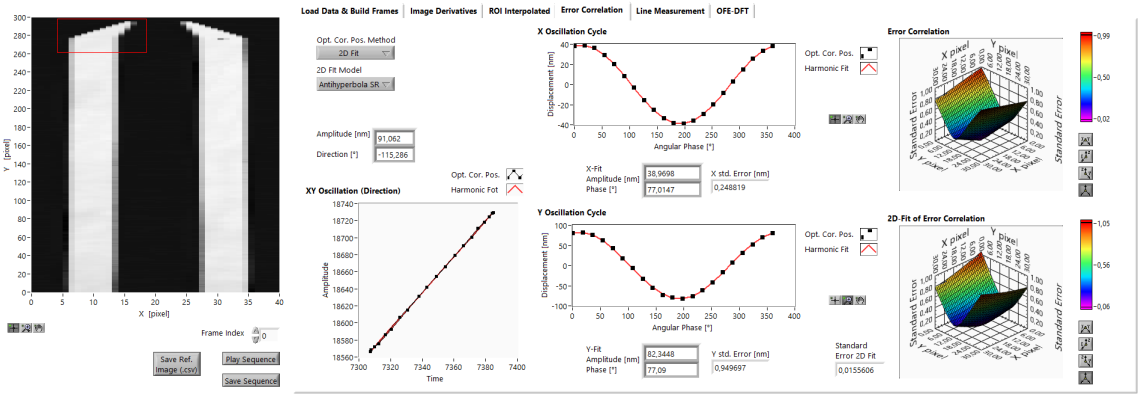

Figure D.4: Error Correlation of selected ROI

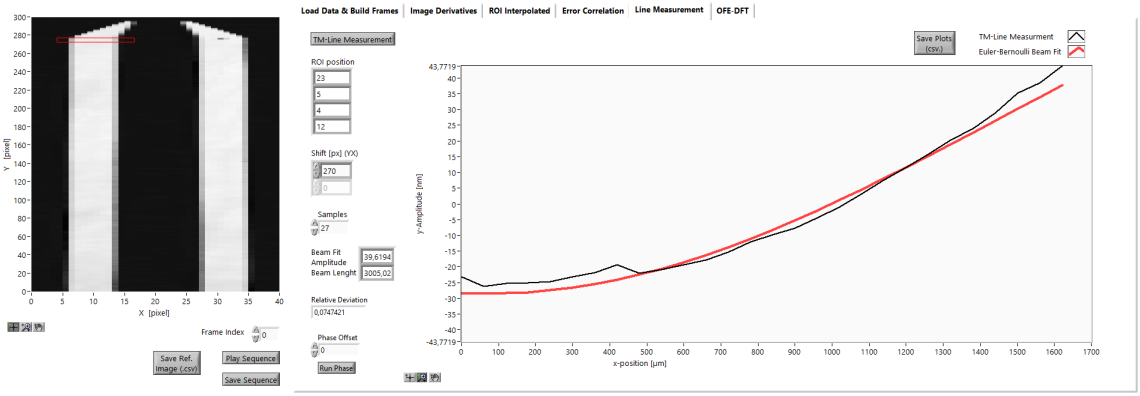

Figure D.5: Line measurement using EC on a defined path of ROIs

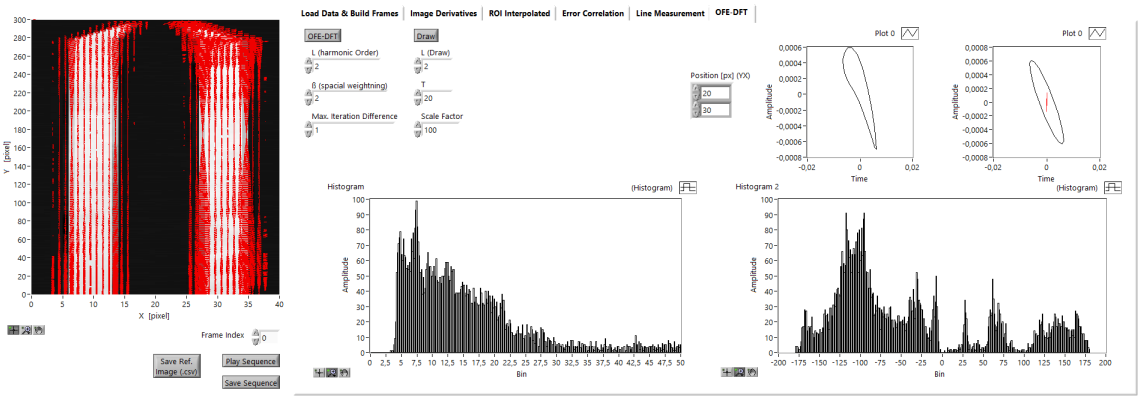

Figure D.6: OFEPIS-algorithm results

Appendix E

Eidesstattliche Erklärung

Hiermit versichere ich, dass ich diese Arbeit selbständig verfasst und keine anderen als die angegebenen Quellen und Hilfsmittel benutzt habe. Außerdem versichere ich, dass ich die allgemeinen Prinzipiem wissenschaftlicher Arbeit und Veröffentlichung, wie sie in den Leitlinien guter wissenschaftlicher Praxis der Carl von Ossietzky Universität Oldenburg festgelegt sind, befolgt habe.

I hereby certify that I have written this work independently and have used no other than the specified sources and aids. I also assure that I have followed the general principles of scientific work and publication as declared in the guidelines of good scientific practice of the Carl von Ossietzky university of Oldenburg.

Datum / Ort Unterschrift